

AD-A234 289

GL-TR-90-0267

**System Concept and Analysis of an
Artificial Ionospheric Mirror (AIM) Radar**

Robert D. Short
Clayton V. Stewart
Tom Wallace
Pierre Lallement
Peter Koert

ARCO Power Technologies, Inc.
1250 Twenty Fourth St., NW
Suite 850
Washington, DC 20037

31 August 1990

Scientific Report No. 1

Approved for Public Release, Distribution Unlimited

Geophysics Laboratory
Air Force Systems Command
United States Air Force
Hanscom Air Force Base, MA 01731-5000

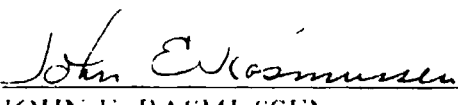
DTIC
ELECTE
APR 8 1991
S B D

DTIC FILE COPY

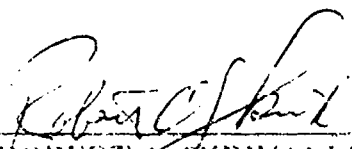
01 4 05 084

"This technical report has been reviewed and is approved for publication"


JOHN L. HECKSCHER
Contract Manager


JOHN E. RASMUSSEN
Branch Chief

FOR THE COMMANDER


ROBERT A. SKRIVANEK
Division Director

This report has been reviewed by the FSD Public Affairs Office (PA) and is releasable to the National Technical Information Service (NTIS).

Qualified requestors may obtain additional copies from the Defense Technical Information Center. All others should apply to the National Technical Information Service.

If your address has changed, or if you wish to be removed from the mailing list, or if the addressee is no longer employed by your organization, please notify GI/TMA, Hanscom AFB, MA 01731. This will assist us in maintaining a current mailing list.

Do not return copies of this report unless contractual obligations or notices on a specific document require that it be returned.

REPORT DOCUMENTATION PAGE		Form Approved OMB No. 0704-0188	
<small>1. This report was prepared by the contractor under contract to the Department of Defense. It contains information which may be classified as "Secret" or "Confidential". It is to be controlled in accordance with the instructions appearing hereon and the instructions appearing in the accompanying document. The contractor shall ensure that all personnel who have access to this report are aware of its classification and control requirements. The contractor shall also ensure that all personnel who have access to this report are aware of the fact that this report is unclassified and that it is to be controlled in accordance with the instructions appearing hereon.</small>			
1 AGENCY USE ONLY (leave blank)	2. REPORT DATE 31 August 1990	3. REPORT TYPE AND DATES COVERED Scientific No. 1 89/8/31 to 90/8/31	
4. TITLE AND SUBTITLE System Concept and Analysis of an Artificial Ionospheric Mirror (AIM) Radar		5. FUNDING NUMBERS C: F19628-89-C-0174 PE: 62101F PR: 4643 TA: 10 WU: AM	
6. AUTHOR(S) R. Short, C. Stewart, T. Wallace, P. Lallement, and P. Koert			
7. PERFORMING ORGANIZATION NAME(S) AND ADDRESS(ES) ARCO Power Technologies, Inc. 1250 Twenty-Fourth St., NW Suite 850 Washington, DC 20037		8. PERFORMING ORGANIZATION REPORT NUMBER APTI-5005	
9. SPONSORING MONITORING AGENCY NAME(S) AND ADDRESS(ES) Geophysics Laboratory Hanscom Air Force Base, MA 01731-5000 Contract Manager: J. Heckscher/LID		10. SPONSORING MONITORING AGENCY REPORT NUMBER GL-TR-90-0267	
11. SUPPLEMENTARY NOTES			
12a. DISTRIBUTION AVAILABILITY STATEMENT Approved for public release, distribution unlimited.		12b. DISTRIBUTION CODE	
13. ABSTRACT Recognition of performance limitations associated with traditional skywave over-the-horizon (OTH) high frequency (HF) radars has led a number of investigators to propose the creation of an Artificial Ionospheric Mirror (AIM) in the upper atmosphere, in order to reflect ground-based radar signals for OTH surveillance. The AIM is produced by beaming sufficient electromagnetic power to the lower ionosphere (around 70 km) to enhance the in situ ionization level to $10^7 - 10^8$ electrons/cm ³ , thereby providing an ionized layer capable of reflecting radar frequencies of 30 - 90 MHz. This paper presents a baseline AIM system concept and an associated performance evaluation, based upon the relevant ionization and propagation physics and in the context of air surveillance for the cruise missile threat. Results of the subject study indicate that a system using this concept would both complement and enhance the performance of the existing skywave OTH radars.			
14. SUBJECT TERMS Artificial Ionospheric Mirror, Over-the-Horizon Radar, Surveillance Radar		15. NUMBER OF PAGES 52 16. PRICE CODE	
17. SECURITY CLASSIFICATION OF REPORT Unclassified	18. SECURITY CLASSIFICATION OF THIS PAGE Unclassified	19. SECURITY CLASSIFICATION OF ABSTRACT Unclassified	20. LIMITATION OF ABSTRACT UL

Table of Contents

1.0 AIM System Concept	1
2.0 AIM Formation and Control.....	4
2.1 Background.....	4
2.2 Vertical Electron Density Profile Control.....	4
2.3 Heater Control Errors.....	7
2.3.1 Sensitivity Relationships	8
2.3.2 Sensitivity Trade-offs.....	12
2.4 AIM Variations Due to Finite Step Heater Scanning.....	13
2.4.1 Analysis Of Stepped Beam Induced Density Fluctuations	15
2.4.2 An Illustrative Example.....	18
2.4.3 Quantitative Results.....	21
3.0 AIM Propagation Effects	24
3.1 Background	24
3.2 Absorption and Dispersion Losses.....	27
3.2.1 Absorption	27
3.2.2 Dispersion Loss	31
3.3 AIM Lifetime and Wind Effects	35
3.3.1 AIM Lifetime	35
3.3.2 Wind Effects	35
3.4 Faraday Rotation	36
4.0 Projected Threat and AIM System Performance	39
4.1 The Cruise Missile Threat.....	39
4.2 A Baseline System and Its Predicted Performance	40
5.0 Summary	44
6.0 Acknowledgements.....	45
7.0 Bibliography	46

Accession For	
NTIS GRA&I	<input checked="" type="checkbox"/>
DTIC TAB	<input type="checkbox"/>
Unannounced	<input type="checkbox"/>
Justification	
By _____	
Distribution/	
Availability Codes	
Dist	Avail and/or Special
A-1	

1.0 AIM System Concept

Strategic defense of the continental United States (CONUS) depends upon our ability to detect and track potential threats approaching at long ranges, allowing adequate time for assessment and reaction. To address this critical need for early warning surveillance, well beyond the line of sight (LOS) of traditional radars, the U.S. Air Force has developed and is currently operating the Over-the-Horizon Backscatter (OTH-B) radar surveillance system (AN/FPS-118) [1]. In addition to OTH-B, the U.S. Navy has developed the Relocatable Over-the-Horizon Radar (ROTHR), the AN/TPS-71 [2,3]. Operational results from the initial east coast facility indicate that OTH-B will serve as a valuable cornerstone to the early warning surveillance capability required for CONUS defense. The threats of particular current interest are penetrators that exhibit small radar cross sections, including air launched and submarine launched cruise missiles (ALCM and SLCM). This threat will become more important in theater warfare as well over the next few decades. The ability to supplement current wide area surveillance with reliable, all weather, continuous detection and tracking of low flying, low observable targets is paramount to the successful implementation of both strategic and tactical air defense strategies.

Recognition of the performance limitations associated with the natural ionosphere motivated a number of investigators (eg. A. Drobot and D. Papadopoulos; A. V. Gurevich [4,5]) to propose the creation of an Artificial Ionospheric Mirror (AIM) in the upper atmosphere, in order to reflect ground-based radar signals for OTH surveillance. The AIM is produced by beaming sufficient electromagnetic power to the lower ionosphere (around 70 km) to enhance the in situ ionization level to $10^7 - 10^8$ electrons/cm³, thereby providing an ionized layer capable of reflecting radar frequencies of 5 - 90 MHz. This paper presents a baseline AIM system concept and an associated performance evaluation, based upon the relevant ionization and propagation physics in the context of air surveillance for the cruise missile threat. Results of the subject study indicate that a system using this concept would both complement and enhance the performance of the existing skywave OTH radars, as illustrated in Figure 1. Performance analyses for the projected system show that it has the potential for providing reliable and consistent detection and tracking of the cruise missile threat.

The performance characteristics of a stand-alone AIM system are highlighted by

- 200-1200 km detection/tracking ranges (depending on target altitude),
- azimuth coverage over 360°, or any fractional sector,
- beam grazing angles of less than 10 degrees (for 65-80 km high AIM),
- good horizontal polarization control,
- operation at RF's in the HF to low VHF (to about 90 MHz), and
- 90% detection probability of a -25 dBsm target at 1,000 km range, providing 30 dB of margin for typical low observable threat projections at VHF.

The performance of a normal skywave OTH system can be enhanced by providing an additional AIM sector (Figure 2), which has sustained operation in the 20-30 MHz regime independent of time of day, latitude, look angle, and ionospheric state. The introduction of an AIM, located at the appropriate altitude, will create a reliable and predictable reflection of the HF energy between the radar site and the area of interest. An AIM adjunct to a conventional HF skywave radar can offer substantially improved performance with regard to:

- filling in the range hole that exists out to about 1000 km due to the minimum HF hop distance,
- mitigation of auroral effects in polar directed surveillance sectors,

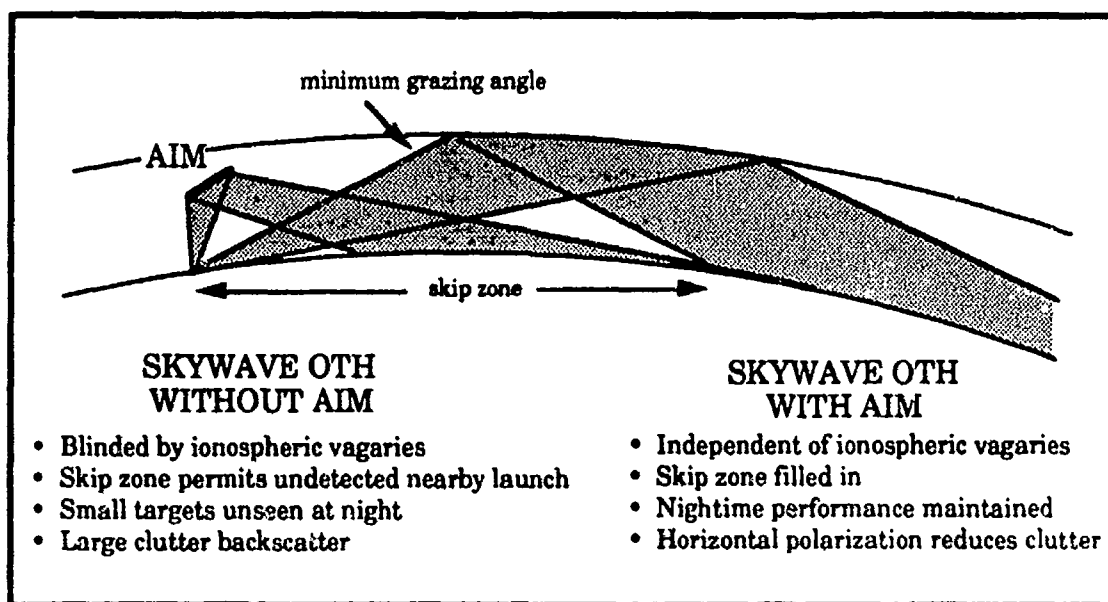


Figure 1. An AIM-Based Radar Will Serve as a Valuable Complement to a Skywave OTH Radar

- sustained operation through periods of increased sunspot activity and other ionospheric degradations,
- availability of the upper end of the HF spectrum during the diurnal ionospheric cycle, and
- improved detection of LO targets through frequency selection and positive polarization control.

In addition, an AIM based system is not restricted to the HF band, but can operate in the lower VHF band, which has several advantages over HF:

- less crowded band permits broader bandwidths, resulting in better resolution and increased sensitivity.
- lower noise temperature, allows higher signal-to-noise ratios and improved detection performance.
- resonant frequencies for cruise missile types of targets, allowing long range detection of otherwise very difficult to detect threats, as illustrated in Figure 2.

Specific issues influencing an AIM system design fall into one of three primary categories:

- AIM heater design trade-offs, which determine how well one can control the production of an AIM layer,
- AIM RF propagation effects, which allow one to assess the quality of the reflected radar wave (eg. absorption, wavefront distortions, doppler spreading, and Faraday rotation), and
- Environmental and operational requirements, which specify the threat and mission context in which the AIM system must perform.

This report will present results concerning each of these issues, highlighting and quantifying those most critical in determining the bottom-line radar system performance.

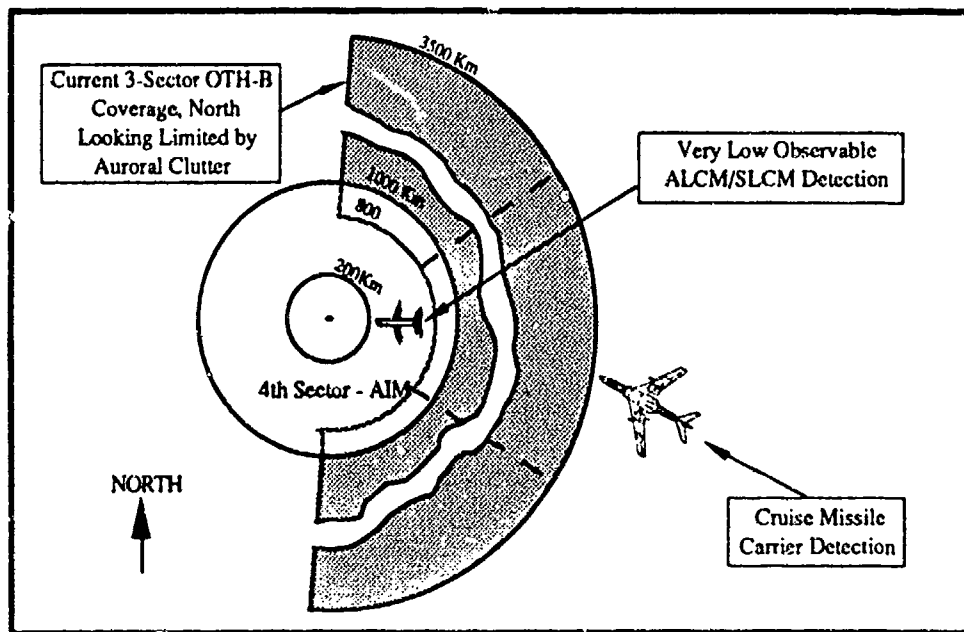


Figure 2. AIM Provides an Additional High Resolution, Highly Available Surveillance Sector

2.0 AIM Formation and Control

2.1 Background

Results from theoretical analysis and numerical modelling indicate that a useful AIM consists of an ionized layer, with an electron density gradient increasing with altitude from the ambient state to a density with plasma frequency corresponding to the radar frequency. The AIM layer is oriented with an inclination ($\sim 40^\circ$ - 45°) and has a slight curvature to allow the radar wave to refract over a 15° elevation beamwidth, providing range coverage from 200 to 1,200 km. In addition, the AIM azimuth orientation is incrementally stepped over the desired angle of surveillance.

Figure 3 illustrates the system timing dependence between the AIM heater operation and the surveillance sequence of the radar. The illustration shows the time coordination of the AIM heater and the radar at three time scales. The coarsest scale (bottom) indicates the sequence of patch creation, followed by radar dwell. Using this strategy, the direction of the radar dwell can be changed at each dwell (by creating a new patch orientation), thereby achieving a scanning radar beam. The middle time-line shows a single AIM creation/dwell period, in which the AIM is created (approximately 10 to 50 ms), followed by a short cooling time (less than .1 ms), and a radar dwell for the life of the cloud (~ 1 s). The size and orientation of the AIM relative to the spot size of the focussed RF heater beam (~ 36 m diameter for this case) requires that the AIM creation be performed with a raster scanning procedure. Figure 3 illustrates the time sequence for this scanning procedure, in which a complete AIM is formed by moving the heater focus along a stepped sequence of horizontal sweeps (each sweep produces a bar of ionization the width of the patch and takes ~ 70 to $350 \mu\text{s}$). The altitude at which ionization occurs is determined by where the power density exceeds the breakdown threshold. Positive control of this altitude is achieved by using a large, partially filled, array and focussing the beam so that the AIM is formed on the front side of the focus. The focal position is controlled so as to follow a surface contour having the desired azimuth and elevation orientation and a slight curvature to allow for radar beam divergence over the azimuth elevation required for surveillance. This procedure is referred to as "painting" and is notionally illustrated in Figure 4. Based on our current understanding of ionization physics and current technology, a typical AIM will require on the order of a 10 to 50 ms to paint.

A central issue concerned with evaluating the feasibility of the AIM concept is how reliably one can create the AIM within tolerances necessary for useful reflection of the radar signal. Issues that directly impact usefulness include: size, shape, orientation, uniformity, smoothness, peak electron density, steepness of the density gradient, and density lifetime. In order to adequately address these issues, one needs a comprehensive understanding of the phenomenology (validated experimentally) and a careful analysis of the heater system design parameters as they impact plasma formation control. The underlying physics has been a major focus of study and the results are reported in [6]. The system trade-off considerations indicate that the AIM can be created using current technology, with the necessary radar reflective characteristics to provide wide area surveillance and early detection and tracking of the ALCM/SLCM threat of the future. Specific results of the system trade-off studies are presented in the following discussions.

2.2 Vertical Electron Density Profile Control

As indicated above, altitude control of the AIM formation is achieved by utilizing a large focussed heater array, so that ionization begins on the front edge of the focus (power density is increasing with altitude). Breakdown initiates where the power density reaches a threshold level (30 kW/m^2 @ 69 km altitude and heater frequency, $f_h = 425 \text{ MHz}$), and rapidly increases in ionization rate above this level. As the number of electrons increase, absorption of the heater wave begins to

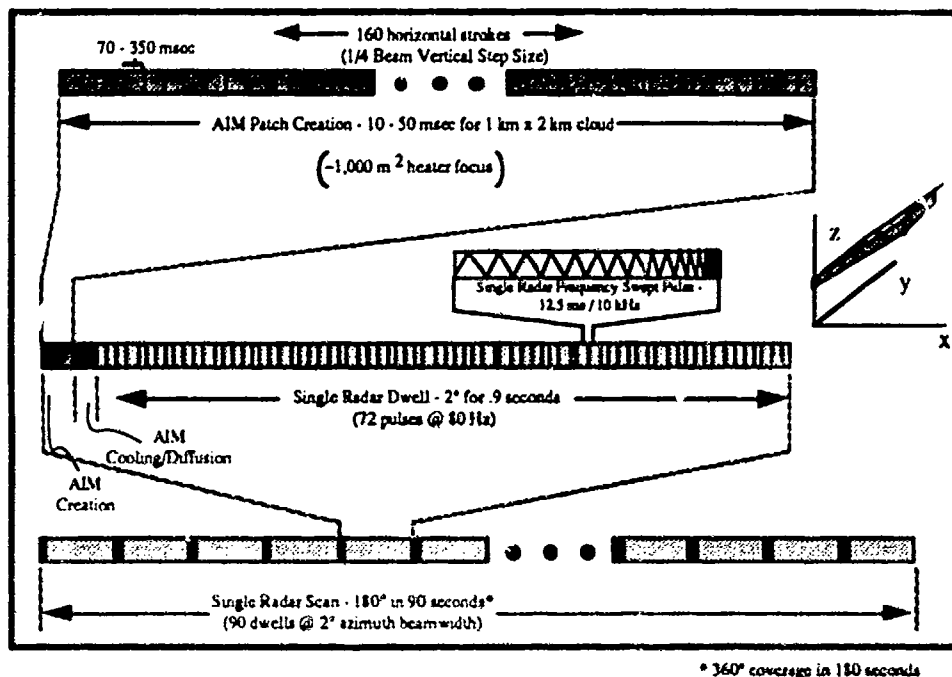


Figure 3. AIM System Timing Diagram

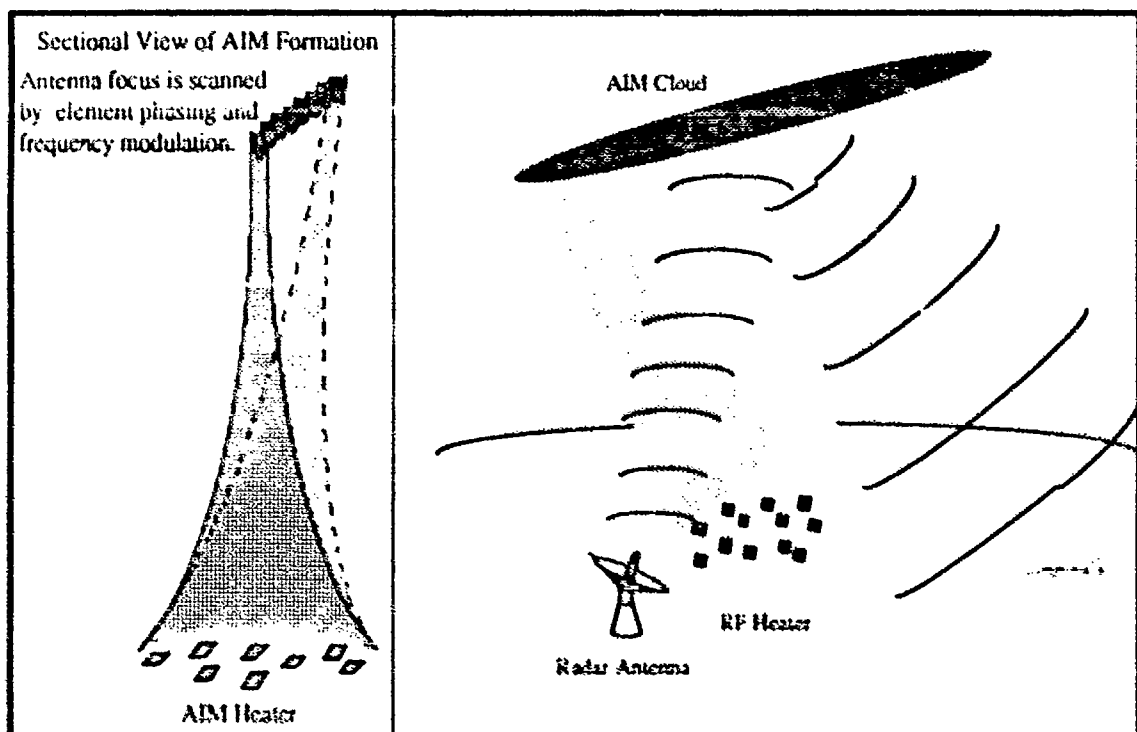


Figure 4. The Large, Sparse Heater Can Paint a Smooth, Homogeneous AIM Patch

reduce the power reaching altitudes above the critical altitude and continues reducing the power level until it drops below the threshold. This "self-absorption" mechanism limits ionization levels to plasma frequencies well below the heater frequency. Figure 5 illustrates a time evolution of the ionization process as a function of altitude. This figure clearly shows the limiting of the peak density and the steepening of the electron density profile over time. This steepening is due to the fact that self-absorption causes the ionization to stop at the higher altitudes first and then to walk back toward the critical altitude. Upon examination of the graph, we note that the critical power density for this situation is approximately 45 dBW/m². Moreover, when the power density has attenuated below 42 dBW/m² at 70 km altitude, there is no further ionization at that altitude.

While many factors impact the resulting electron density profile, the major influencing factors, within control of the system designer, are the heater frequency, dwell time, and the power density gradient. Increasing the heater frequency reduces the absorption rate, thereby allowing higher peak plasma densities. Longer dwell time allows the the profile to walk further back toward the critical altitude, hence increasing the final density gradient. The third factor, power density gradient, determines how rapidly the power density is increasing beyond the threshold density and consequently how much absorption is required to reduce the field strength down to the critical level. While higher power density gradients produce higher peak plasma frequencies, increased gradients are obtained at the expense of smaller beam widths and thus smaller ionization areas. Approximate relationships between these factors and the electron density profile parameters have been empirically determined for AIM formation at 70 km altitude [7]. The peak electron density is

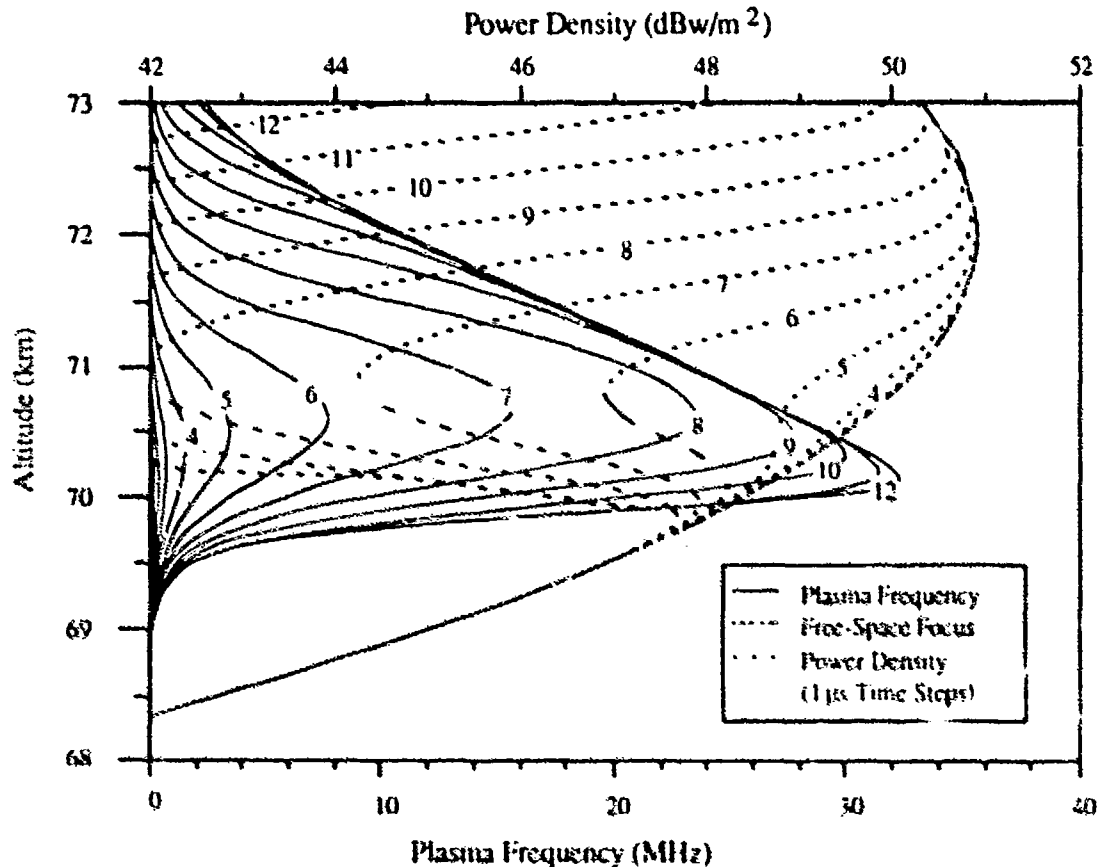


Figure 5. Growth Through Time of AIM Cloud with $f_h = 425$ MHz, $\tau = 12 \mu s$ ($1 \mu s$ step size)

$$N_e = \min \left\{ N_{eo} 1.5 \exp \left(8.4 \times 10^{-12} \left(P_f / f_h^2 \right)^2 \tau \right), 2 \times 10^7 f_h^{2.1} \nabla P_z^{1.5} \right\} \quad (1)$$

and the electron density gradient is

$$\frac{dN_e}{dz} = \min \left\{ 14 \exp \left(6.5 \times 10^{-6} \tau^{.58} P_f / f_h^2 \right), 7.5 \times 10^4 f_h^{1.35} \max \{ \nabla P_z, 4 \} \right\}, \quad (2)$$

where

- P_f = power density at the power peak (W/m²)
- f_h = heater frequency (GHz)
- τ = pulse length (μsec)
- N_{eo} = ambient electron density (cm⁻³) = 10² cm⁻³ at 70 km
- ∇P_z = power density gradient at the electron density peak (dB/km).

In each case the first term in $\min\{\cdot, \cdot\}$ represents the growth phase of the cloud, while the second term represents the maximum or clamped state of the cloud. As τ increases, the growth formula approaches and finally reaches the value of the clamped formula, at which point the second term becomes the valid expression. Since these relationships are only valid for a neutral density corresponding to 70 km altitude, in order to support a full system design trade-off, they will be expanded to account for altitude dependence (ie. sensitivity to neutral density).

As will be discussed in Section 3.0, these profile characteristics have important implications relative to utilizing the AIM as an RF reflector, determining both the maximum useable frequency (MUF) and the amount of absorption and wavefront distortion incurred while the wave transits the cloud. Therefore, the AIM system engineer must carefully trade-off the relevant heater characteristics and resulting performance degradations against overall cost considerations. In order to adequately perform such a trade-off, the relation between heater/AIM characteristics and system performance must be quantified. Quantification of two major factors is discussed in the following two subsections, while the remaining issues are addressed in Section 3.0.

2.3 Heater Control Errors

As mentioned above, formation of the AIM plasma will be achieved by RF radiation from a very large ground-based phased array. Since neutral density and electron density spatial variations are less than .05% over AIM scale lengths [8], the primary source of plasma irregularities will be due to heater scanning and control. The objective of the following analysis and associated discussion is to derive and evaluate some rough measures of sensitivity between the inherent uncertainties in generating the individual heater element waveforms, the resulting perturbations in AIM breakdown location, and subsequent impact on radar system performance. Deviations in waveform generation at the element level result in corresponding deviations in the desired power density profile in the breakdown region. Three specific potential sources of error are considered:

- simple additive noise,
- amplitude distortions, and
- phase distortions.

While the following discussion specifically addresses issues related to a large digitally controlled solid state heater, the results can be readily applied to high power microwave sources.

Examples of potential causes of these errors include quantization errors in the digital circuitry, digital-to-analog conversion errors, power amplifier gain deviations and distortions, and timing errors in the waveform control circuitry. Each of these factors is considered relative to what is readily achievable with current technology and how these performance limitations impact the patch integrity.

Results of this analysis indicate that although the power density/breakdown dependencies require relatively accurate control of the power density profile (e.g. to within .003 dB, which corresponds to a SNR at the focal point of 68 dB), the large number of independent heater elements results in significant integration gains (e.g. a configuration of 40,000 elements reduces the 68 dB requirement at the focal point by 46 dB to only 22 dB at the element level). A summary of the impact of this integration gain on what is achievable with currently available hardware technology is summarized in Table 1.

Table 1. Heater Error Budget Achievable with Currently Available Hardware

Error Factor	Deviation in AIM Location
Quantization Noise	0.13 m
D/A Noise	.009 m
Power Amplifier Distortions	< .13 m
Phase Deviations	.33 m
Cumulative Error (Worst Case)	.36 m

For the surveillance radar frequency operating at 50 Mhz, the patch irregularities indicated by the cumulative error is on the order of .06 wavelengths. As indicated by Greene's analysis [9], an aperture with rms phase errors of this order of magnitude will experience minimal performance degradation (less than .3 dB reduction in gain, less than .2% increase in beamwidth, and root-mean-square (rms) beam canting less than 10% of the beamwidth). Furthermore, when path averaging of the radar wave within the plasma is taken into account, the results indicate that the net effect on radar performance is negligible (~ .02 dB).

In the following discussion, we derive the relationship between element waveform errors and the resulting error in plasma breakdown location. Each potential error source is related to an equivalent element waveform error. These two relationships are then combined to determine the sensitivity of the AIM breakdown location to each noise factor. The consequent AIM location errors are used in Section 3.0 to evaluate the impact these factors have on radar detection.

2.3.1 Sensitivity Relationships

Figure 6 illustrates the basic patch-heater geometry with the indicated parameters defined as:

- \underline{r} = desired location of the array focus, relative to the center of the heater.
- \underline{r}_n = location of the n th heater element, relative to the center of the heater.
- $E(\underline{r}, t)$ = desired electric field at location \underline{r} and time t .
- $E_n(t)$ = desired element waveform.
- $g(\hat{\phi})$ = element amplitude gain pattern, and
- $\hat{\phi}_n = (\underline{r} - \underline{r}_n)/|\underline{r} - \underline{r}_n|$, unit direction vector from the n th element.

For a heater array with N elements and c denoting the speed of light, the ideal electric field intensity is given by the summed contributions from each element.

$$\begin{aligned}
 E(\underline{r}, t) &= \sum_{n=1}^N g(\hat{\phi}_n) \frac{E_n(t - |\underline{r} - \underline{r}_n|/c)}{4\pi|\underline{r} - \underline{r}_n|^2} \\
 &= \frac{E_0}{4\pi|\underline{r}|^2} \sum_{n=1}^N g(\hat{\phi}_n) E_n(t - |\underline{r} - \underline{r}_n|/c).
 \end{aligned}
 \tag{3}$$

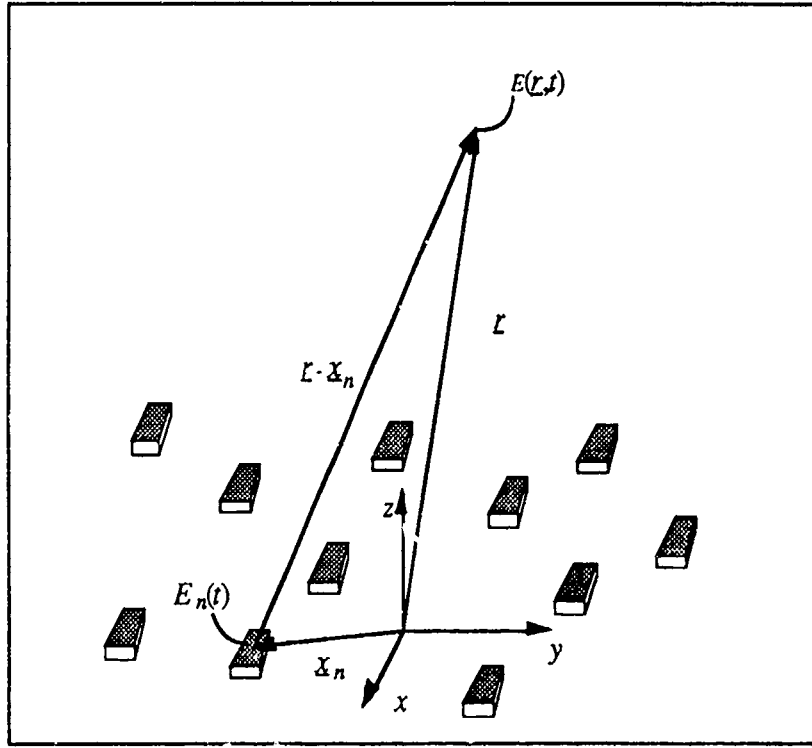


Figure 6. Geometry of Heater Array Sensitivity Analysis

where \underline{L} is the polarization orientation of the electric field and $\|\underline{L}\| \gg \|\underline{x}_n\|$.

Equation (3) provides the relationship between the electric field intensity at location \underline{L} and the ideal element waveforms. For a non-ideal waveform, we assume that $g(\phi_n)E_n(t)$ has been perturbed by an additive noise process, η_n , which has zero mean and variance $\mathbb{E}\{|\eta_n(t)|^2\} = \sigma_\eta^2$, where $\mathbb{E}\{\cdot\}$ denotes the statistical expectation. The actual contribution to $\underline{E}(\underline{L}, t)$ by each element is

$$g(\phi_n)E_n(t) + \eta_n(t).$$

In the analysis to follow, we assume the element errors are uncorrelated from element to element. This appears to be a reasonable assumption for the error sources mentioned above.¹ Given this assumption, the desired power density and potential noise power at the focal point of the heater are

$$P_f = \mathbb{E}\{|\underline{E}(\underline{L}, t)|^2\} = \frac{1}{2} N^2 E^2 \quad (4)$$

and

$$\sigma_f = \mathbb{E}\left\{\left|\sum_{n=1}^N \eta_n(t)\right|^2\right\} = N \sigma_\eta^2. \quad (5)$$

In equations (4) and (5) we have approximated the $1/\|\underline{L} - \underline{x}_n\|^2$ spreading loss to be the same for each element, thus omitting the common $1/(4\pi R^2)$ factors from (4) and (5). In addition, to

¹ One possible exception is the timing circuitry. Timing errors due to system clock jitter would correlate across all of the heater elements. This is discussed in more detail at a later point in the paper.

simplify the analysis, we assume that E_n is generated such that the magnitude of the $g(\phi_n)E_n$ are equal ($|g(\phi_n)E_n| = E$). Combining (4) and (5) gives the signal-to-noise ratio (SNR) of the power density at the focal point of the heater

$$SNR = \frac{N|E|^2}{2\sigma_\eta^2} = N SNR_e, \quad (6)$$

where SNR_e is the signal-to-noise ratio at the output of each individual heater element.

In order to relate the SNR at the focus of the array to resulting irregularities in the patch breakdown location, we will consider the effects of deviations from the desired power density profile on breakdown location. Figure 7 illustrates a representative power density profile in one dimension with the corresponding plasma electron density after breakdown. In the region of breakdown, the power density is approximated by

$$10 \log_{10}(P) = \alpha z + \beta, \quad (7)$$

where z is the altitude from the heater array. Using (7), a small deviation in power, ΔP , will result in an altitude offset, Δz ; representing the difference between the desired location, at which the power density reaches the critical breakdown level, P_c , and the actual location of the critical power density,

$$\Delta z = \frac{10}{\alpha} \log_{10}\left(1 + \frac{\Delta P}{P_c}\right). \quad (8)$$

A linear approximation in (8) gives

$$\Delta z \approx \frac{10}{\alpha \ln(10)} \frac{\Delta P}{P_c}. \quad (9)$$

If the $\eta_n(t)$'s are independent random processes, the central limit theorem implies that Δz is a non-central chi-squared random variable, with mean and variance derived from (9)

$$\mathbf{E}\{\Delta z\} = \frac{10}{\alpha \ln(10)} \cdot \frac{\sigma_e^2}{P_c} \quad (10)$$

and

$$\sigma_{\Delta z}^2 = \left[\frac{10}{\alpha \ln(10)} \right]^2 \frac{\sigma_e^2}{P_c} \left(1 + \frac{\sigma_e^2}{2P_c} \right) \approx \left[\frac{20}{\alpha \ln(10)} \right]^2 SNR_e^{-1}. \quad (11)$$

In (10) and (11), σ_e^2 represents the variance in the combined field error at the breakdown altitude, due to all elements and SNR_e is the signal to noise ratio at the breakdown point. SNR_e will be less than at the focus, because defocussing of the elements causes the expected field intensity to be reduced, while the sum of independent element errors is not affected by the phase difference between elements. Combining equations (6), (10), and (11) gives the variance in the error between the average breakdown location, z_c , and the actual location, $z_c + \Delta z$.

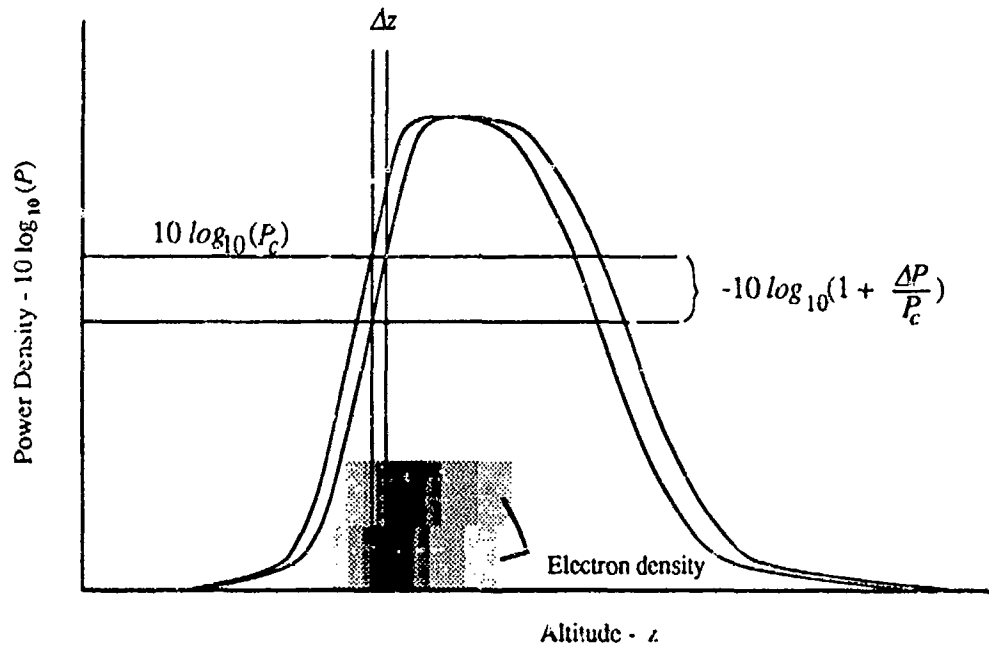


Figure 7. Illustration of the Breakdown Dependence Upon Power Density Perturbations

$$\sigma_{\Delta z} = \frac{20}{\alpha \ln(10) \sqrt{N \xi SNR_e}}, \quad (12)$$

where ξ is the relative amount of focus (ie. P_c/P_f).

In order to use (12) as the basis for evaluating the impact of potential heater array errors on patch location, each of the error sources to be evaluated must be tied to an equivalent additive noise error. For small scale errors, the three potential sources of error can be related to SNR_e as shown in Table 2. In Table 2, $\gamma(t)$ corresponds to the relative amplitude distortion (i.e. 100 σ_γ is the percent rms distortion) and $\psi(t)$ is the absolute phase error.

Table 2. Equivalent Additive Element Noise ξSNR_e 's for Three Classes of Errors¹

Additive Noise $\eta(t)$	Amplitude Distortion $\gamma(t)$	Phase Error $\psi(t)$
$\xi \frac{ E ^2}{2\sigma_\eta^2}$	$\frac{\xi}{\sigma_\gamma^2}$	$\frac{\xi}{(e^{\sigma_\psi^2/2} - e^{-\sigma_\psi^2/2})}$

¹ The SNR_e 's have been derived by assuming that 1) the amplitude distortion produces an electric field intensity from each element of $E_n(1 + \epsilon_n)$, where ϵ_n is a zero mean error and E_n includes the element phasing and 2) the phase error produces an element field intensity $E_n \exp(-\sigma^2/2) + E_n (\exp(j\psi_n) - \exp(-\sigma^2/2))$, where the first term is the average value and the second is the random zero-mean perturbation about the average. In each case, the first and second terms are summed over all elements and the mean and variance calculated. The ratio of the squared mean to the variance forms the resulting SNR_e , dividing this by the number of elements gives the equivalent SNR_e .

2.3.2 Sensitivity Trade-offs

In this section we combine the results of Table 2 with equation (12) to obtain a family of trade-off curves that indicate the expected rms AIM location error as a function of the error contributions of the four classes of error sources. For a given error budget assigned to each contributing factor, the total rms error can be found by

$$\sigma_{\Delta z}^2 = \sqrt{\sigma_{\Delta z_1}^2 + \sigma_{\Delta z_2}^2 + \sigma_{\Delta z_3}^2}, \quad (13)$$

where $\sigma_{\Delta z_i}^2$ is the error variation due to factor i . Figure 8 shows the dependence of the breakdown location error on the element signal-to-noise ratio for three different power density gradients. Expressing the noise levels for $\eta(t)$ and $\chi(t)$ in dB relative to the unperturbed waveform, the impact of these perturbations on Δz can be assessed directly from Figure 8. Figure 9 gives the sensitivity of Δz to the phase error, $\psi(t)$.

Table 3 provides an assessment of the achievable performance levels using currently available technology. These numbers have been obtained from vendor specification data sheets and in-house experience with related hardware. The cumulative rms error from all factors in Table 3 provide a rms deviation in breakdown altitude of no more than .36 meters. This corresponds to a rms deviation across the AIM patch of less than .06 wavelengths for a 50 Mhz radar frequency.

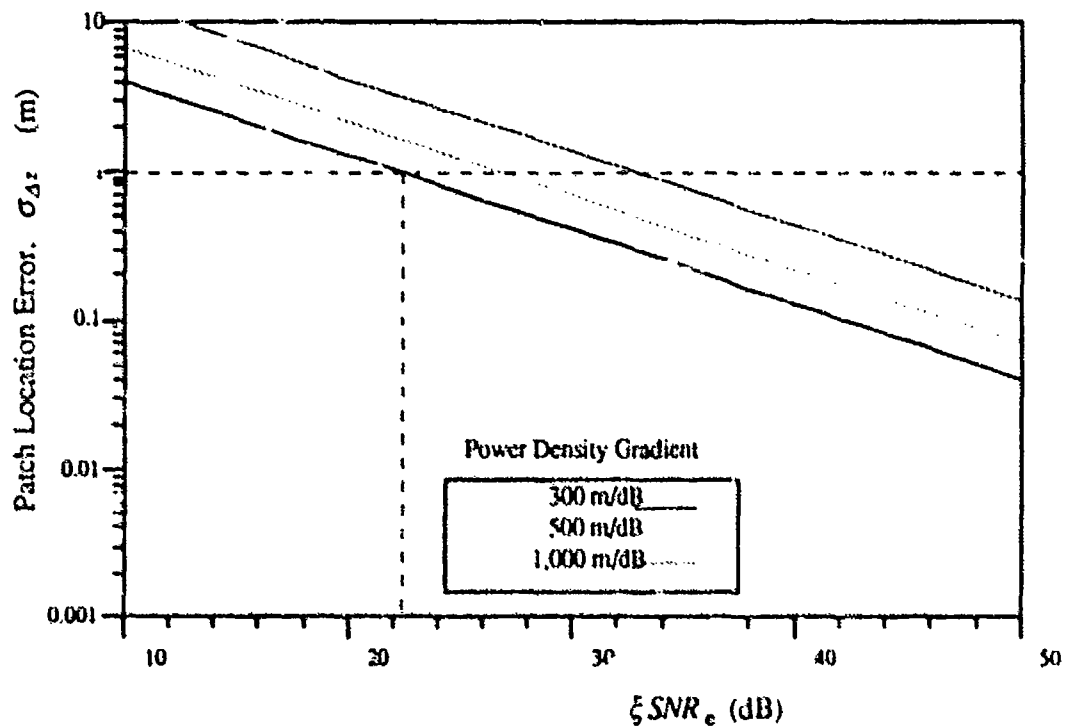


Figure 8. Sensitivity of Breakdown Location to Heater Element Signal-to-Noise Ratio

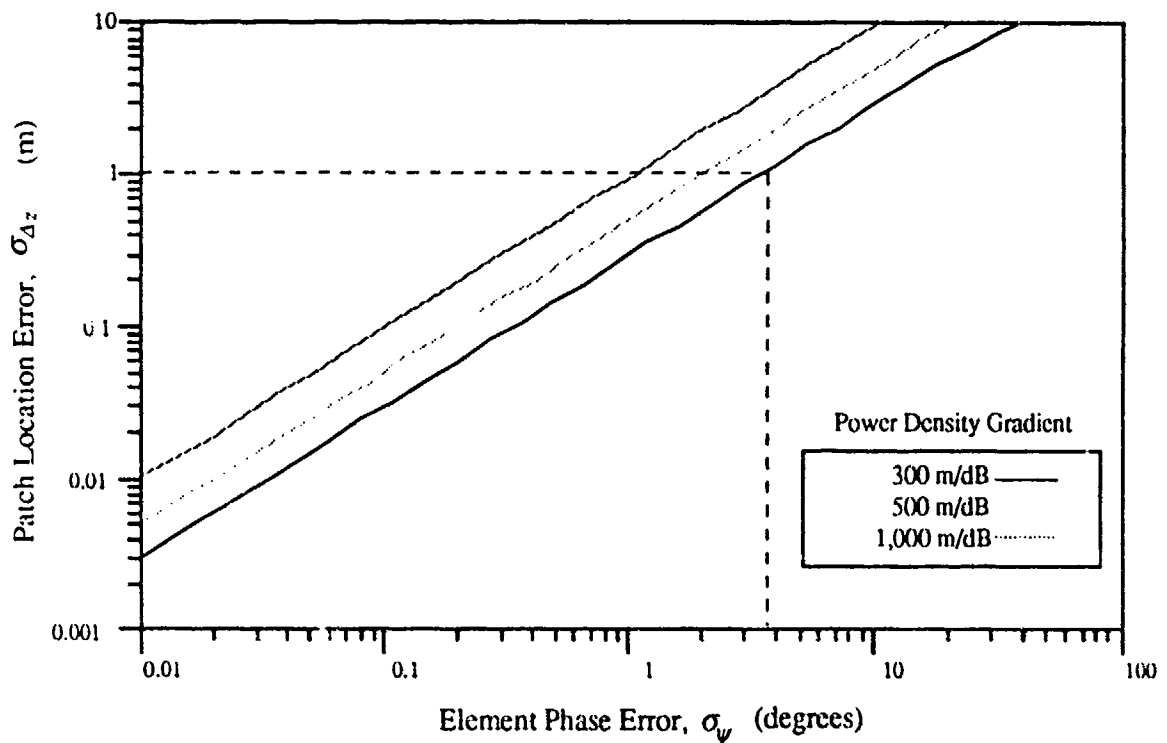


Figure 9. Sensitivity of Breakdown Location to Heater Element Phase Errors

Table 3. Impact of Achievable Heater Element Performance Factors on AIM Breakdown

Error Factor	Achievable Performance	Equivalent SNR_e	Δz rms ¹
Quantization Noise	10 to 12 bits	60 dB	.018 m
D/A Noise	$\sim \frac{1}{2}$ bit	63 dB	.013 m
System Clock Jitter	$\sim \frac{1}{3}^\circ$ @ 350 Mhz	N/A ²	N/A
Power Amplifier Distortion	< -40 dB THD @ 350 Mhz	> 40 dB	< .17 m
Phase Deviations	< 1° rms	> 35 dB	.33 m

2.4 AIM Variations Due to Finite Step Heater Scanning

In the following discussion, we address the issue of AIM irregularities due to the heater's finite step beam motion in the direction of the AIM inclination. Figure 10 illustrates the step scanning of the heater beam along a short segment of the AIM contour. In this figure, the heater dwells for a given time, τ seconds, and then steps the focal point a third of a beamwidth in the cross beam direction and a corresponding distance in the bore-sight direction. This dwell and step process is repeated for the extent of the AIM. As Figure 10 shows, while the desired constant electron density contour is a line inclined at 45° , the actual contour due to the quantization of the beam step has a ripple that oscillates about the desired contour. This irregularity in the AIM will produce a

¹ Assumes breakdown power is 3 dB below the focus, $\xi = 1/2$.

² System clock jitter will affect all elements uniformly and will therefore result in a timing error, but not a power density perturbation.

corresponding ripple in the phase front of the refracted radar wave. The extent of wavefront ripple will depend both upon the magnitude of the contour ripple, as well as the depth of the plasma density. A deeper plasma provides more refraction and correspondingly more smoothing of the AIM irregularity, thus less phase front distortion.

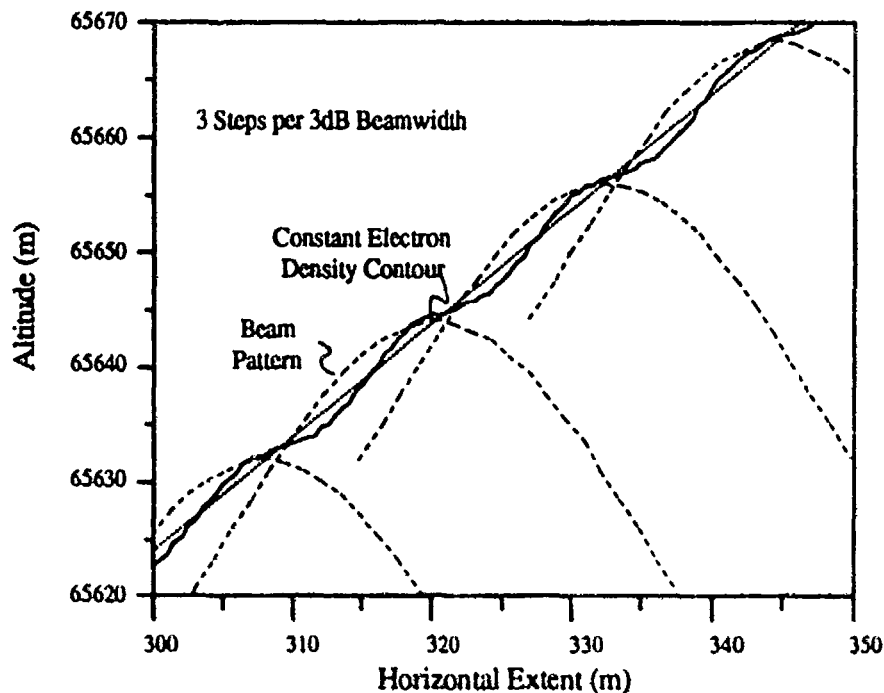


Figure 10. Illustration of Heater Step Scanning

The objective of this section is to quantify the magnitude of these contour fluctuations and determine what beam step sizes are required for acceptable radar performance. These irregularities are studied both from a theoretical perspective, as well as from a straight-forward numerical simulation of the heater step scanning and consequent ionization along the desired constant electron density contour. Quantitative results are provided for the analytic derivations and compared to electron density irregularities produced by the numerical simulation. These results indicate that, within the nominal parameter regime for the current AIM conceptual design,

- 1) the magnitude of electron density irregularities falls off rapidly for paint step sizes less than $1/2$ beam width and
- 2) a $1/4$ beam step size produces a density fluctuation with magnitude less than .1% of the average and a corresponding location fluctuation less than .1 m.

The next section presents a derivation of the analytic relationships. These relationships are then used in Section 2.4.1 to derive trade-off expressions for a specific heater beam example. Section 2.4.2 uses this result to present a quantitative trade-off between beam step size and resulting density fluctuations. In addition, Section 2.4.2 compares the theoretical results with a numeric simulation of a stepped heater beam and associated ionization.

2.4.1 Analysis Of Stepped Beam Induced Density Fluctuations

In the following discussion, the heater array is assumed to be centered at $(x, z) = (0, 0)$ and is painting a patch by stepping the beam focus from $(-D_x/2, z_f - \gamma D_x/2)$ to $(D_x/2, z_f + \gamma D_x/2)$. As Figure 11 illustrates, each step moves the beam uniformly in x and z , $(\delta x, \delta z) = (\Delta, \gamma \Delta)$.

The power density of the heater¹ can be described at the n th beam step by

$$P_n(x, z) = P_f g(x - n\Delta, z - n\Delta\gamma), \quad (14)$$

where $g(x, z)$ is the heater beam relative gain pattern ($g(0, z_f) = 1$) in the (x, z) coordinates and P_f is the heater power density at the focus. For a step size $\Delta = \frac{D_x}{N}$, the cumulative energy per square meter is found by summing the contribution of each beam dwell at (x, z)

$$E(x, z) = \sum_{n=-N/2}^{N/2} P_o g(x - n\Delta, z - n\Delta\gamma) \tau. \quad (15)$$

To simplify the following analysis, we assume that $g(x, z)$ in the region of the focus is a function of a weighted distance between the point (x, z) and the focal point $(0, z_f)$,

$$g(x, z) = g(ax^2 + b(z - z_f)^2), \quad (16)$$

where a and b determine the focal spread along the x and z axes respectively (ie. the beamwidth and width of focus respectively).

While this form is not completely general, it does allow for a wide class of beam patterns, such as $\exp(-d^k)$ and $\left(\frac{\sin d}{d}\right)^k$ in the focal region of the beam, where $d = \sqrt{ax^2 + b(z - z_f)^2}$. For a pattern satisfying (16), we can show that

$$g(x - n\Delta, z - n\Delta\gamma) = g\left(\frac{ab[x\gamma - (z - z_f)]^2}{a + b\gamma^2} + (a + b\gamma^2)\left[n\Delta - \frac{ax + b\gamma(z - z_f)}{a + b\gamma^2}\right]^2\right). \quad (17)$$

and, for a contour in the (x, z) plane defined by $(z - z_f) = \zeta + \gamma x$, we have

$$g(x; \zeta) = g\left(\frac{ab\zeta^2}{a + b\gamma^2} + (a + b\gamma^2)\left(n\Delta - x - \frac{b\gamma}{a + b\gamma^2}\zeta\right)^2\right). \quad (18)$$

¹ In this analysis we have ignored the effects of self absorption on the heater wave. While this is an important phenomenon during the patch creation process (leading to the self-limiting nature of the peak electron density), the effect on the fluctuation appears to be one of limiting the electron density to some maximum. This will lead to fluctuations in practice that are less than those predicted here.

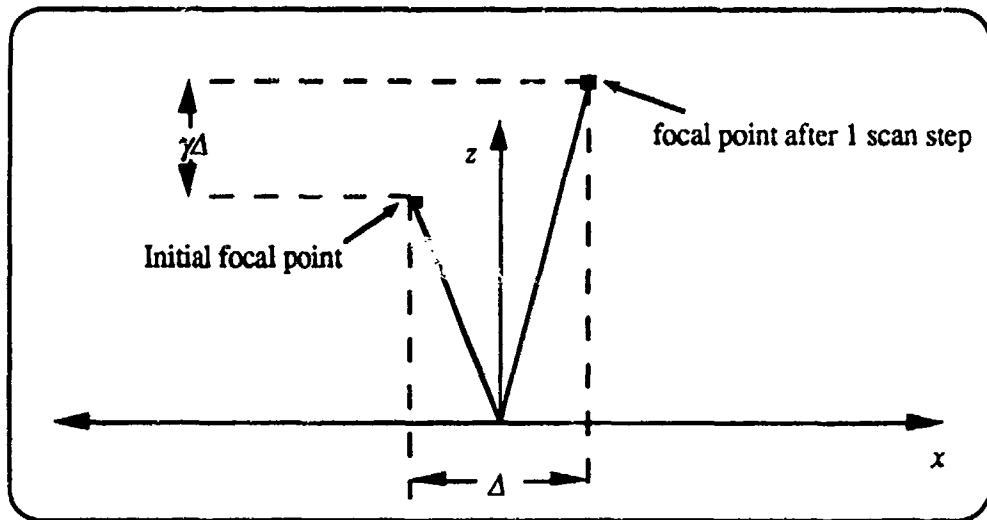


Figure 11. Geometry of Beam Scanning Effects Study

If we now define

$$h(u; \zeta) = g \left(-\frac{ab\zeta^2}{a + b\gamma^2} + (a + b\gamma^2)u^2 \right), \quad (19)$$

the energy flux per square meter along the contour can be approximated by

$$\begin{aligned} \mathcal{E}(x, z) &= \sum_{n=-\infty}^{\infty} P_o h \left(n\Delta - x - \frac{b\gamma}{a + b\gamma^2} \zeta; \zeta \right) \tau \\ &= \tau P_o \int_{-\infty}^{\infty} h \left(u - x - \frac{b\gamma}{a + b\gamma^2} \zeta; \zeta \right) \sum_{n=-\infty}^{\infty} \delta(u - n\Delta) du \\ &= \tau P_o \int_{-\infty}^{\infty} h \left(u - x - \frac{b\gamma}{a + b\gamma^2} \zeta; \zeta \right) \sum_{n=-\infty}^{\infty} \exp(j2\pi \frac{n}{\Delta} u) du \\ &= \tau P_o \sum_{n=-\infty}^{\infty} H^*(n/\Delta; \zeta) \exp \left(j2\pi \frac{n}{\Delta} x + j2\pi \frac{n}{\Delta} \frac{b\gamma\zeta}{a + b\gamma^2} \right) \\ &= \tau P_o \left[H(0; \zeta) + \sum_{n=1}^{\infty} 2H(n/\Delta; \zeta) \cos \left(2\pi \frac{n}{\Delta} x + \phi_n(\zeta) \right) \right]. \end{aligned} \quad (20)$$

In Equation (20) $H(f; \zeta)$ is the Fourier transform of $h(u; \zeta)$ in the u variable,

$$H(f; \zeta) = \int_{-\infty}^{\infty} h(u; \zeta) \exp(-j2\pi fu) du. \quad (21)$$

Equation (20) shows that the energy flux along contours parallel to the AIM surface consists of an average flux, $\tau P_0 H(0; \zeta)$, and a fluctuation with period equal to the beam step size. The Fourier coefficients of the fluctuation are given by the Fourier transform of the beam pattern at frequencies $\frac{n}{\Delta}$. For beam patterns and step sizes of interest to us, the majority of fluctuation is contained in the first harmonic, $f_x = 1/\Delta$. From (20), the first harmonic ripple relative to the average is

$$\delta_{\epsilon} = \frac{2H(1/\Delta; \zeta)}{H(0; \zeta)}. \quad (22)$$

While the energy flux represented by Equation (20) is related to the ionization rate and consequent electron density, the relationship is highly nonlinear and therefore (20) only gives a sense of how the resulting density irregularities will depend upon the heater step size. Derivation of a more accurate relationship follows.

The electron ionization rate has been shown to have the following dependence on heater power density

$$v_{\text{net}} = 9 \times 10^{-9} N \left(\frac{P}{P_c} \left(1 + \frac{v_{\text{max}}^2}{\omega^2} \right) \right) \exp \left[-4.16 \sqrt{\frac{P_c}{P} \left(1 + \frac{v_{\text{max}}^2}{\omega^2} \right)} \right] (1 - G(P/P_c)) \quad (23)$$

$$G(P/P_c) = 3.7 \times 10^{-4} \exp[7.9 \sqrt{P_c/P}],$$

where N is the ambient neutral density, P_c is the critical power density required for breakdown, where the ionization equals reattachment (ie. $(1 - G(1)) = 0$). Along the ζ contour the power density is given by $P_0 h(u; \zeta)$, therefore the ionization rate at location x, ζ during the n th beam dwell can be written as a function of $\frac{P_0}{P_c} h(u; \zeta)$,

$$v_i(x; \zeta, n) = v \left(\frac{P_0}{P_c} h \left(n\Delta - x - \frac{b\gamma}{a + b\gamma^2} \zeta; \zeta \right) \right). \quad (24)$$

Since the buildup of electron density in the regime of interest for AIM is of the cascade type, it is described by an exponential function of $\int v_i(t) dt$. Using (24) for the ionization rate during the n th beam dwell and letting $N_a(x, \zeta)$ denote the ambient electron density, the electron density after the complete heater scan is

$$\begin{aligned}
N_e(x; \zeta) &= N_a(x; \zeta) \exp \left(\sum_{n=-N/2}^{N/2} v \left(\frac{P_e}{P_c} h \left(n\Delta - x - \frac{b\gamma}{a + b\gamma^2} \zeta; \zeta \right) \right) \tau \right) \\
&= N_a(x; \zeta) \exp \left(\tau \left\{ V(0; \zeta) + \sum_{n=1}^{\infty} 2 V(n/\Delta; \zeta) \cos \left(2\pi \frac{n}{\Delta} x + \phi_n(\zeta) \right) \right\} \right) \\
&= N_a(x; \zeta) \exp \left(\tau V(0; \zeta) \right) \left\{ 1 + \tau \sum_{n=1}^{\infty} 2 V(n/\Delta; \zeta) \cos \left(2\pi \frac{n}{\Delta} x + \phi_n(\zeta) \right) \right\},
\end{aligned} \tag{25}$$

where

$$V(f; \zeta) = \int_{-\infty}^{\infty} v \left(\frac{P_e}{P_c} h(u; \zeta) \right) \exp(-j2\pi fu) du. \tag{26}$$

The steps for deriving (25) are analogous to Equation (20). Equation (25) shows that the electron density along contours parallel to the AIM surface will exhibit fluctuations due to heater beam step scanning. These fluctuations have a period equal to the beam step size, Δ , with a relative first harmonic fluctuation magnitude proportional to the beam dwell time and the value of the Fourier transform in (26) at $f_x = 1/\Delta$. If we let the average electron density on contour ξ be defined as

$$N_{e,ave} = N_a(x; \zeta) \exp(\tau V(0; \zeta)), \tag{27}$$

the relative fluctuation in the first harmonic is

$$\begin{aligned}
\delta N_e &= \frac{\delta N_e}{N_{e,ave}} \\
&= \tau 2 V(1/\Delta; \zeta) \\
&= \ln \left(\frac{N_{e,ave}}{N_a(x; \zeta)} \right) \frac{2 V(1/\Delta; \zeta)}{V(0; \zeta)}.
\end{aligned} \tag{28}$$

Equation (28) corresponds to the ratio of the peak electron density fluctuation along the desired constant density contour to the average density. In order to quantify (28), we must specify a heater beam pattern, $g(ax^2 + b(z-z_f)^2)$, an ionization rate $v_i(P)$, and then evaluate the Fourier transform in Equation (26). While this process does not explicitly account for the change in beam pattern due to absorption, it does quantify the density variation during pre-clamping stages of ionization.

2.4.2 An Illustrative Example

In the following discussion we use the results in Section 2.4.1 with a specific heater beam pattern to develop explicit relationships for Equations (22) and (28). For the purpose of illustration we assume a Gaussian beam pattern in the focal region of the heater. For a 3 dB half-width of B_x and B_z in the x and z directions respectively, the heater beam pattern is expressed as

$$g(x, z) = \exp \left(\ln \left(\frac{1}{2} \right) \left(\frac{x^2}{B_x^2} + \frac{(z - z_f)^2}{B_z^2} \right) \right). \tag{29}$$

Using (16) and (29) to identify the appropriate expressions for a and b , (29) can be written in the same form as (16); hence, equation (19) gives

$$h(u; \zeta) = \exp\left(\frac{\ln\left(\frac{1}{2}\right)\zeta^2}{B_z^2 + \gamma^2 B_x^2}\right) \exp\left(\frac{\ln\left(\frac{1}{2}\right)(B_z^2 + \gamma^2 B_x^2)}{B_z^2 B_x^2} u^2\right). \quad (30)$$

The Fourier transform of (30) in the u variable may be performed analytically, producing

$$H(f; \zeta) = \sqrt{\frac{\pi B_z^2 B_x^2}{-\ln\left(\frac{1}{2}\right)(B_z^2 + \gamma^2 B_x^2)}} \exp\left(\frac{\ln\left(\frac{1}{2}\right)\zeta^2}{B_z^2 + \gamma^2 B_x^2}\right) \exp\left(\frac{\pi^2 B_z^2 B_x^2}{\ln\left(\frac{1}{2}\right)(B_z^2 + \gamma^2 B_x^2)} f^2\right). \quad (31)$$

Substituting (31) into (22) and simplifying gives the relative energy fluctuation along the AIM surface contour

$$\delta_E = \frac{2H(1/\Delta; \zeta)}{H(0; \zeta)} = 2 \exp\left(\frac{\pi^2}{\ln\left(\frac{1}{2}\right)} \frac{B_z^2 B_x^2}{B_z^2 + \gamma^2 B_x^2} \left(\frac{1}{\Delta}\right)^2\right). \quad (32)$$

Figure 12 shows a plot of δ_E as a function of $\frac{2B_x}{\Delta}$, the number of heater scanning increments per beamwidth. Although this plot is for specific parameter values, $B_x = 36$ m and $B_z = 2,700$ m, the results are widely applicable across the potential operational regime of the AIM heater, since, for $B_x \ll B_z$,

$$\delta_E = 2 \exp\left(\frac{\pi^2}{4 \ln\left(\frac{1}{2}\right)} \left(\frac{2B_x}{\Delta}\right)^2\right). \quad (33)$$

As Figure 12 illustrates, the fluctuation in ionization energy along a constant density contour becomes extremely small, for even moderate beam overlapping; for example, with only 2 increments per beamwidth the fluctuation in energy is 59 dB below the average energy. As will be seen below, these low energy fluctuations translate into correspondingly low electron density fluctuations.

In order to obtain a closed form expression for the ionization rate and resulting electron density, we will approximate the ionization rate by a Kth order polynomial in $\frac{P_a}{P_c}$. Substituting (30) into (33), defining ζ_c such that $P_c = P_a \cdot g(\zeta_c)$, and using the polynomial approximation,

$$\begin{aligned} \sqrt{\frac{P_a}{P_c}} &= N_a A \sum_{k=1}^K a_k \left(\frac{P_a}{P_c}\right)^k \\ &= N_a A \sum_{k=1}^K a_k \left[\exp\left(k \ln\left(\frac{1}{2}\right) \left(\frac{\zeta^2}{B_z^2 + \gamma^2 B_x^2} - \frac{\zeta_c^2}{B_z^2}\right)\right) \right. \\ &\quad \left. \cdot \exp\left(\frac{k \cdot \ln\left(\frac{1}{2}\right) \cdot (B_z^2 + \gamma^2 B_x^2)}{B_z^2 B_x^2} u^2\right) \right] \end{aligned} \quad (34)$$

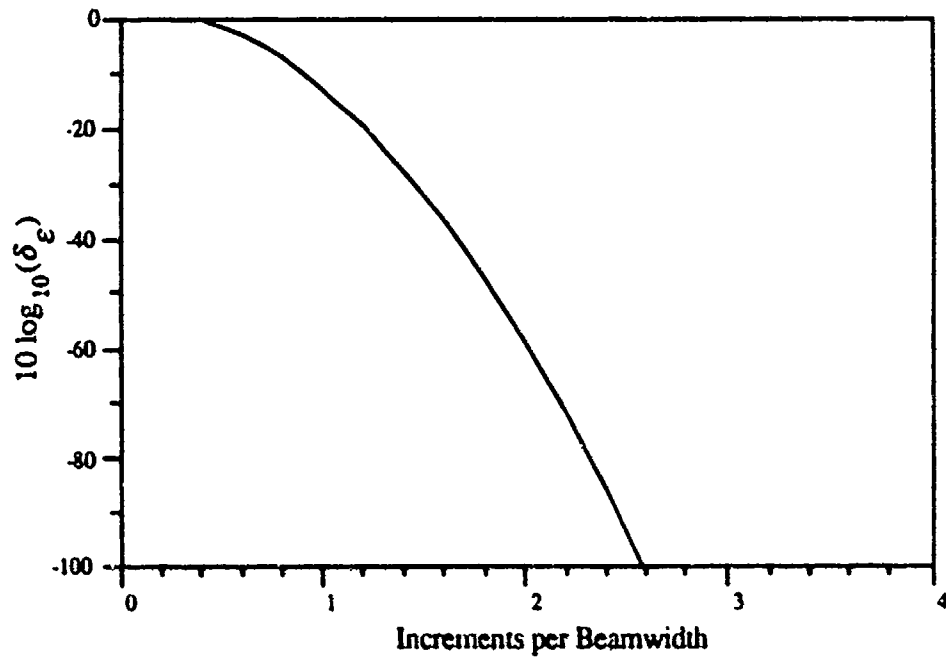


Figure 12. Fluctuation in Energy Flux Versus Scanning Increment

Substituting equation (34) into (26) and performing the integration gives the following Fourier transform of ν :

$$N(f, \zeta) = N_o A \sqrt{\frac{\pi B_x^2 B_z^2}{-\ln\left(\frac{1}{2}\right)(B_x^2 + \gamma^2 B_z^2)}} \cdot \sum_{k=1}^K \frac{a_k}{\sqrt{k}} \left| \exp\left(k \ln\left(\frac{1}{2}\right) \left(\frac{\zeta^2}{B_x^2 + \gamma^2 B_z^2} - \frac{\zeta^2}{B_x^2} \right) \right) \exp\left(\frac{\pi^2 B_x^2 B_z^2}{k \ln\left(\frac{1}{2}\right)(B_x^2 + \gamma^2 B_z^2)} f^2 \right) \right| \quad (35)$$

Finally, using (35) to evaluate (28),

$$\delta E_i = \ln \left(\frac{N_{e,ave}}{N_a(x; \zeta)} \right) = \frac{2 \sum_{k=1}^K \frac{a_k}{\sqrt{k}} \left| \exp\left(k \ln\left(\frac{1}{2}\right) \left(\frac{\zeta^2}{B_x^2 + \gamma^2 B_z^2} - \frac{\zeta^2}{B_x^2} \right) \right) \exp\left(\frac{\pi^2 B_x^2 B_z^2}{k \ln\left(\frac{1}{2}\right)(B_x^2 + \gamma^2 B_z^2)} \left(\frac{1}{\Delta}\right)^2 \right) \right|}{\sum_{k=1}^K \frac{a_k}{\sqrt{k}} \left| \exp\left(k \ln\left(\frac{1}{2}\right) \left(\frac{\zeta^2}{B_x^2 + \gamma^2 B_z^2} - \frac{\zeta^2}{B_x^2} \right) \right) \right|} \quad (36)$$

As was indicated above, over the parameter regime relevant to AIM, $B_x \ll B_z$; therefore, (36) may be approximated by

$$\delta N_e = \ln \left(\frac{N_{e,ave}}{N_a(x; \zeta)} \right) \frac{2 \sum_{k=1}^K \frac{a_k}{\sqrt{k}} \left(\exp \left(\frac{k \ln \left(\frac{1}{2} \right)}{B_z^2} (\zeta^2 - \zeta_c^2) \right) \exp \left(\frac{\pi^2}{4k \ln \left(\frac{1}{2} \right)} \cdot \left(\frac{2B_x}{\Delta} \right)^2 \right) \right)}{\sum_{k=1}^K \frac{a_k}{\sqrt{k}} \left(\exp \left(\frac{k \ln \left(\frac{1}{2} \right)}{B_z^2} (\zeta^2 - \zeta_c^2) \right) \right)} \quad (37)$$

Given a K order polynomial approximation for the ionization rate, Equation (37) gives the relative electron density fluctuation along the desired constant density contour located ζ meters from the heater focus z_f . As (37) demonstrates, the fluctuation is a function of the heater focus dimensions, B_x and B_z , the distance from the focus to the altitude where ionization begins, ζ_c , and the heater step size, Δ . The next section will quantify these fluctuations for a typical set of AIM parameters.

2.4.3 Quantitative Results

A numerical simulation has been performed for a specific set of heater beam parameters. The simulation uses the one dimensional breakdown model, as defined in line 1 of Equation (25), for a fixed value of ζ over a range of x encompassing the patch. Figure 13 shows the results of this simulation over a short segment of the patch for the following heater beam parameters given in Table 4.

The fluctuation level measured for this simulation is compared to the analytic predictions derived in the previous section. In order to quantify Equation (38), a 12th order polynomial approximation to

Table 4. Heater Beam Parameters

Focus altitude:	z_f	72,000 m
Heater spot width at focus:	$2B_x$	36 m
Heater spot focal width (in altitude):	$2B_z$	5,500 m
AIM Contour Distance from focus:	ζ	-4,675 m
Distance from focus where ionization begins:	ζ_c	-5,500 m
Heater step size:	Δ	variable
Time to step through one beamwidth:	$\tau \frac{2B_x}{\Delta}$	55 μsec^1

$v \left(\frac{P}{P_c} \right)$ was derived by selecting polynomial coefficients to minimize the mean-square error, over the power density range of interest. Figure 14 compares the the resulting approximation with the actual curve for Equation (25) over the range .1 to 10. This includes the range of $\frac{P(x, \zeta)}{P_c}$ values along the ζ contour, for which significant ionization occurs. Using the resulting coefficients and substituting the relevant heater parameters into (37) provides a quantitative expression for trading off the heater step size against the resulting level of electron density fluctuation. This relative fluctuation can be translated into a corresponding location perturbation. When the fluctuations are

¹ This time corresponds to an ionization time required for a 300 MHz heater with an ERP of 155 dB, this time is shorter for higher frequency, higher ERP heater configurations.

small scale, perturbations are approximately linear. Therefore, the location perturbation is related to the density gradient by

$$\delta z = \left(\frac{\partial N_e}{\partial z} \right)^{-1} \cdot \delta N_e \cdot N_{e,ave} . \quad (38)$$

For a linear gradient with depth D , (38) is bounded by $\delta z < D \delta N_e$. Figure 15 shows the quantitative tradeoff between the heater's scanning step size and the resulting electron density fluctuation and corresponding altitude fluctuation for the heater parameters given above. As this plot indicates, the density fluctuation drops dramatically as the scan step size decreases below the half beamwidth size. For a $\frac{1}{4}$ beam increment, density fluctuations are less than .1%, with corresponding location errors less than .1 meter.

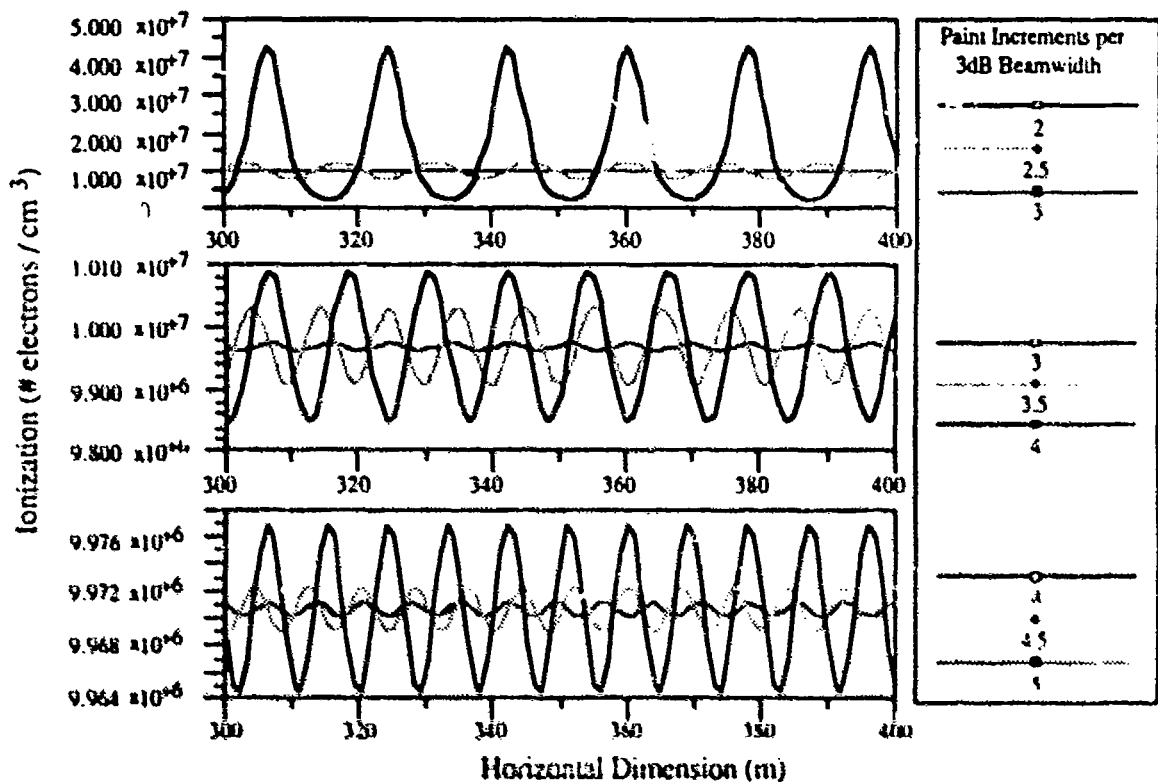


Figure 13. Numerical Simulation Of Electron Density Fluctuations Due to Step Scanning

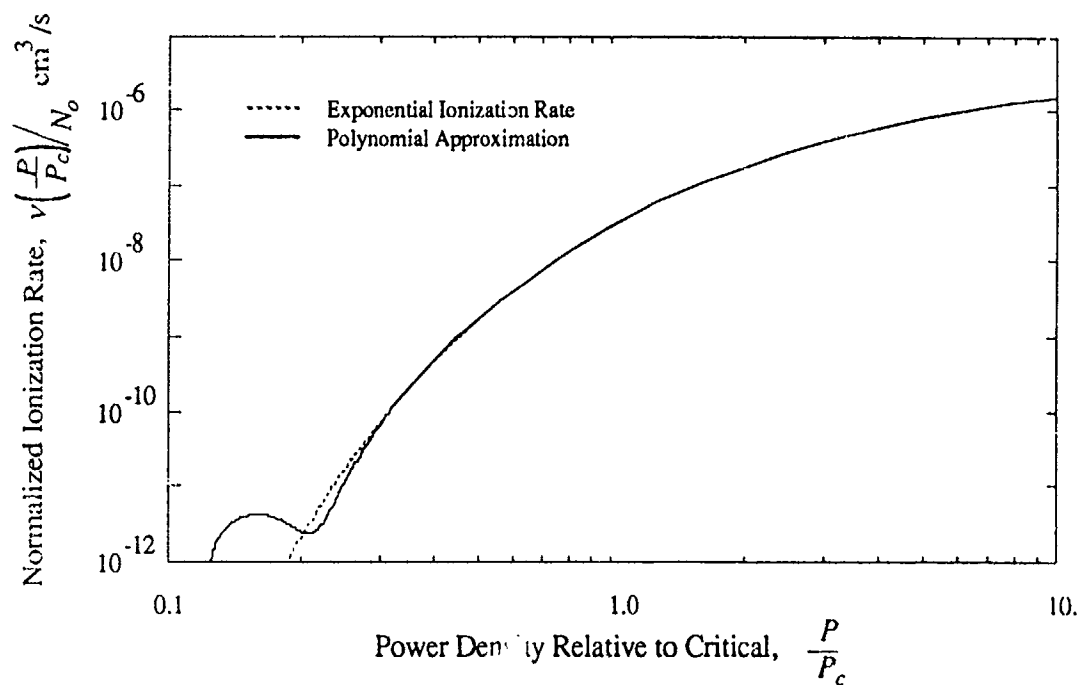


Figure 14. Polynomial Approximation to Ionization Rate

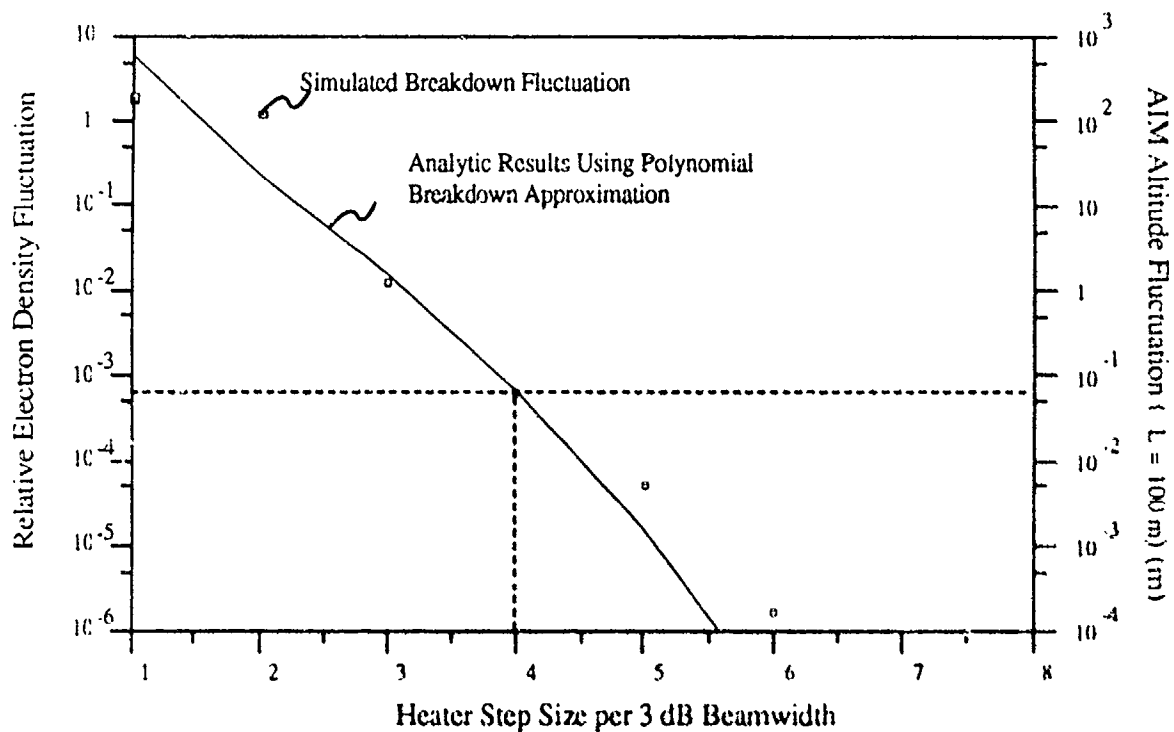


Figure 15. Electron Density Fluctuations Versus Heater Step Size

3.0 AIM Propagation Effects

3.1 Background

We begin our discussion of the radar system performance with a brief derivation of a radar range equation appropriate for AIM detection analysis. The AIM geometry differs from that of a traditional radar by the introduction of the reflecting layer in the propagation path. This layer intercepts the radar beam and refracts the intercepted wave toward the direction of the target. Accounting for the reflecting area, losses during the reflection process, and the two phases of spreading loss (pre- & post-reflection) make up the major difference between an AIM range equation and a line-of-sight, monostatic radar.

The relevant radar system and patch geometry parameters are defined as follows:

Radar System:

- P_t = average transmitted power
- P_r = average received power
- G_t = transmit antenna gain
- A_r = receive aperture
- f = RF frequency (λ = wavelength)
- B = signal bandwidth
- Φ_s = angle of surveillance coverage
- T_s = scan time
- $T_d = T_s \theta / \Phi_s$ (dwell time)
- L_s = radar system losses
- T^* = total effective noise temperature (including atmospheric noise)
- σ_t = target cross section

AIM Geometry/Losses:

- h = AIM altitude
- R = range from the AIM to target
- θ = incident angle at the AIM
- Δ_a = azimuthal dispersion off the AIM
- Δ_e = elevation dispersion off the AIM
- w = AIM width
- l = AIM length
- L_p = AIM one-way absorption
- γ_p = one-way Faraday rotation P_{hv} / P_{hh}

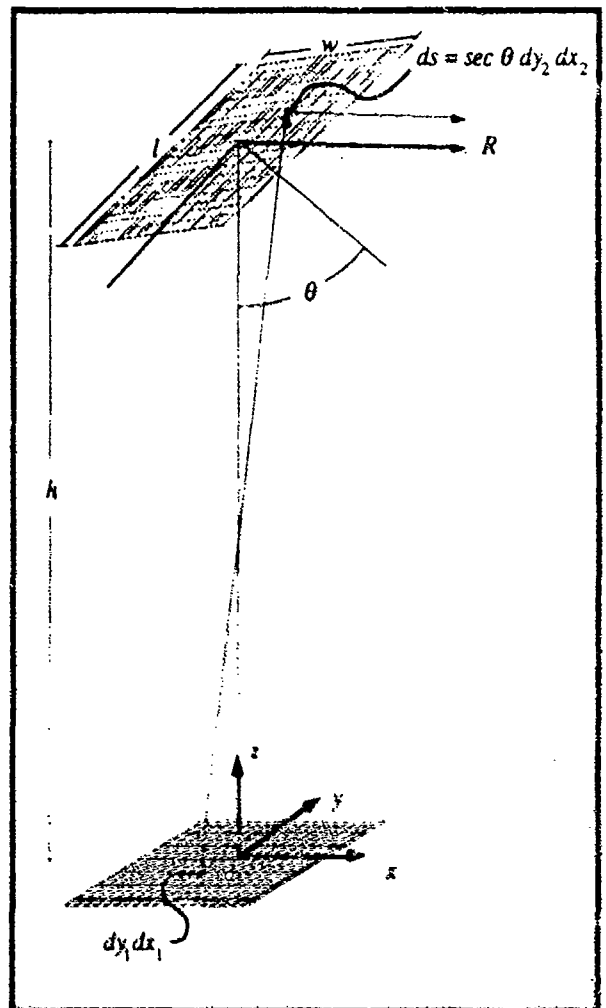


Figure 16. AIM Geometry Parameters

The appropriate expression for received power can be best understood by applying the Fresnel-Kirchhoff diffraction integral across the transmitting aperture to calculate the field at the patch and then across the patch to calculate field reflected through the patch to a target at a distance R from the patch in direction of the reflection angle θ (see Figure 16) [10, 11]. Assuming a constant illumination across the antenna, the resulting integration can be expressed as

$$F(P) = j \iint_{S_p S_x} \frac{\exp(-jk(R_1 + R_2))}{\lambda^2 R_1 R_2} \cos^2 \theta \, ds_x ds_p, \quad (39)$$

where

$$R_1 = h + x_2 \tan \theta - \frac{x_2^2}{2h} \tan^2 \theta + \frac{(x_2 - x_1)^2}{2h} + \frac{(y_2 - y_1)^2}{2h}, \quad (40)$$

$$R_2 = R - x_2 \tan \theta - \frac{x_2^2}{2R} \tan^2 \theta + \frac{x_2^2}{2h} + \frac{y_2^2}{2h}, \quad (41)$$

$ds_x = dx_1 dy_1$, and $ds_p = \sec \theta dx_2 dy_2$. The approximate path lengths in (40) and (41) are used to approximate the relative phase delays (Fresnel approximation), while retention of the first term is adequate for accounting for the $1/R$ spreading loss. Substitution of (40) and (41) into (39) gives

$$|F(P)| = \left| \iint_{S_p S_x} \frac{1}{\lambda^2 h R} \exp \left(jk \left(\frac{x_1 x_2}{h} + \frac{y_1 y_2}{h} \right) \right) \exp \left(-jk \left(\frac{x_1^2 + y_1^2}{2h} + \left(\frac{x_2^2}{2h} + \frac{x_2^2}{2R} \right) (1 + \tan^2 \theta) + \left(\frac{y_2^2}{2h} + \frac{y_2^2}{2R} \right) \right) \right) \cos^2 \theta \, ds_x ds_p \right|. \quad (42)$$

Squaring (42) and multiplying by the transmit power density at the antenna gives the power density at the target. Using the principle of reciprocity, the reflected power from the target can be calculated analogously, where the receive aperture is used in place of the transmit aperture.

The quadratic terms in the phase expression of Equation (42) divide the (w, l, θ, h, R) parameter space into numerous regions, depending upon the relevance of the different quadratic phases to the integral. In general if the quadratic term, $x_2^2 h R / 2 \lambda (h + R) < 1$, then that term can be omitted from the phase argument. Consideration of the relevant range of values for (w, l, θ, h, R) , leads to the consideration of 4 parameter regimes:

$$\begin{aligned}
C1: \frac{(l/2)^2 \cos^2 \theta (h+R)}{2\lambda h R} < .1, \frac{(w/2)^2 (h+R)}{2\lambda h R} < .1 \quad C2: \frac{(l/2)^2 \cos^2 \theta (h+R)}{2\lambda h R} > .1, \frac{(w/2)^2 (h+R)}{2\lambda h R} < .1 \\
C3: \frac{(l/2)^2 \cos^2 \theta (h+R)}{2\lambda h R} < .1, \frac{(w/2)^2 (h+R)}{2\lambda h R} > .1 \quad C4: \frac{(l/2)^2 \cos^2 \theta (h+R)}{2\lambda h R} > .1, \frac{(w/2)^2 (h+R)}{2\lambda h R} > .1
\end{aligned}$$

These cases correspond to the radar antenna being in the Fresnel region (case 4), far-field (case 1), or some combination thereof (cases 2 and 3), relative to the AIM. For example, a 50 MHz radar, with an AIM created at 70km and a target at 1000 km, will come into the Fresnel region when l exceeds 790 m and w exceeds 560 m. These cases are important, because they determine the appropriate form for the field intensity range equation, as follows:

$$\begin{aligned}
C1: |F(P)| &\propto \frac{A_x}{\lambda(h+R)} & C2: |F(P)| &\propto \frac{A_x l \cos \theta}{\lambda^{3/2} \sqrt{hR(h+R)}} \\
C3: |F(P)| &\propto \frac{A_x w}{\lambda^{3/2} \sqrt{hR(h+R)}} & C4: |F(P)| &\propto \frac{A_x w l \cos \theta}{\lambda^2 h R}
\end{aligned}$$

In order to achieve the azimuth and elevation beam spreading consistent with the desired coverage (1.5° to 3° and 15° respectively), the AIM surface profile will be slightly curved. This curvature will cause different portions of the patch to reflect along different azimuth-elevation directions, filling in the entire azimuth-elevation beam. For the purposes of system performance analysis, the propagation can be modelled by assuming that the AIM and radar antenna are both in the far-field with respect to each other (case 4). The resulting model can be partitioned into the four segments of the radar wave's propagation to and back from the target. These four segments are transmitter-to-patch, patch-to-target, target-to-patch, and patch-to-receiver. Each corresponding component of the range equation accounts for the spreading loss, absorption, beam dispersion, and relevant cross sections along the related propagation path. The power density at the end of each segment is summarized by

$$P_r = \left[\frac{P_t G_t}{4\pi h^2} \right] \cdot \left[\frac{A_p G_p}{4\pi R^2} \right] \cdot \left[\frac{\sigma_t}{4\pi R^2} \right] \cdot \left[\frac{A_p G_p}{4\pi h^2} \right] \cdot A_r L_s \quad (43)$$

$$\begin{array}{|c|c|c|c|}
\hline
\text{transmit} & \text{patch} & \text{target} & \text{patch} \\
\hline
\text{-to-} & \text{-to-} & \text{-to-} & \text{-to-} \\
\hline
\text{patch} & \text{target} & \text{patch} & \text{receiver} \\
\hline
\end{array}$$

In (43) the effective AIM reflecting aperture and gain, A_p and G_p respectively, are given by

$$A_p = L_p w l \cos(\theta) \quad (44)$$

and

$$G_p = \frac{4\pi}{\Delta_\alpha \Delta_\epsilon} \quad (45)$$

For a coherent dwell and receiver noise given by kT , the signal-to-noise ratio at the radar is

$$SNR = \frac{P_r T_d}{k T} . \quad (46)$$

Substituting equation (43) into (46) and combining terms gives

$$SNR = \left[\frac{P_t G_t A_p^2 G_p^2 \sigma_t A_r L_s T_d}{(4\pi)^4 h^4 R^4 kT} \right] . \quad (47)$$

Equation (43) assumes that any losses due to Faraday rotation during the wave's transit is negligible (i.e. $\gamma_p \ll 1$). However, in the case of clutter backscatter (particularly sea clutter), even small amounts of rotation can result in significant increases in clutter returns. This is due to the large differences between horizontal and vertical clutter cross sections (σ_{hh} & σ_{vv}). Typical ratios of $\frac{\sigma_{vv}}{\sigma_{hh}}$ are on the order of 20 dB or more. Taking these cross sections into account, the signal-to-clutter ratio (prior to clutter cancellation) for a horizontal transmit and horizontal receive configuration in sea clutter is given by

$$SCR = \frac{\cos(\psi)}{(\sigma_{hh} + \sigma_{vv} \gamma_p^2) \frac{c}{2B} \Delta_a R} , \quad (48)$$

where B is the radar waveform bandwidth, c is the speed of light, and ψ is the grazing angle at the surface. As will be discussed below, the small, predictable amount of polarization rotation imposed by the plasma layer allows an AIM system to exploit the large difference between horizontal and vertical backscatter.

3.2 Absorption and Dispersion Losses

3.2.1 Absorption

The absorption of the radar wave during reflection has a major influence on the design and performance of the radar system, and the need to create patches with low absorption strongly affects the design of the heater system. The absorption of a patch is determined by the electron-neutral collision frequency ν_m , and the distance which a ray travels within the plasma. This distance, in turn, is determined by the radar frequency and the electron density profile.

An intuitive appreciation of the importance of these factors in determining absorption may be gained by examining an analytic result for the power absorption in decibels of a patch whose plasma density varies linearly with distance into the patch, until $\omega_p = \omega$ (plasma frequency equals the radar frequency) at a depth D^1 ,

$$L_p = \exp \left(- \frac{8\pi}{3} \left(\frac{D}{\lambda} \right) \left(\frac{\nu_m}{\omega} \right) \cos^3(\theta) \right) . \quad (49)$$

¹ A derivation of this result can be found in [12].

For typical AIM geometries, the angle of incidence (θ) will be 35-45°. Although a linear plasma density variation is not typical of those expected to be produced by AIM heaters, this expression is useful for the qualitative insight it provides. Since θ is fixed by the geometry, the absorption is determined by D/λ and ν_m/ω ; if their product is small, the overall absorption will be small. For a given radar RF, the minimum value of ν_m/ω is determined by the ambient collision frequency, and D/λ is determined by the focusing capabilities of the heater system.

Immediately after the patch is created, the electron-neutral collision frequency ν_m is very high. The electrons in the patch rapidly (on the order of 1 μ s) transfer their energy to the neutral atmosphere, and the collision frequency returns to its ambient value. The ambient value, which is the lowest possible collision frequency at a given altitude, is shown in Figure 17.

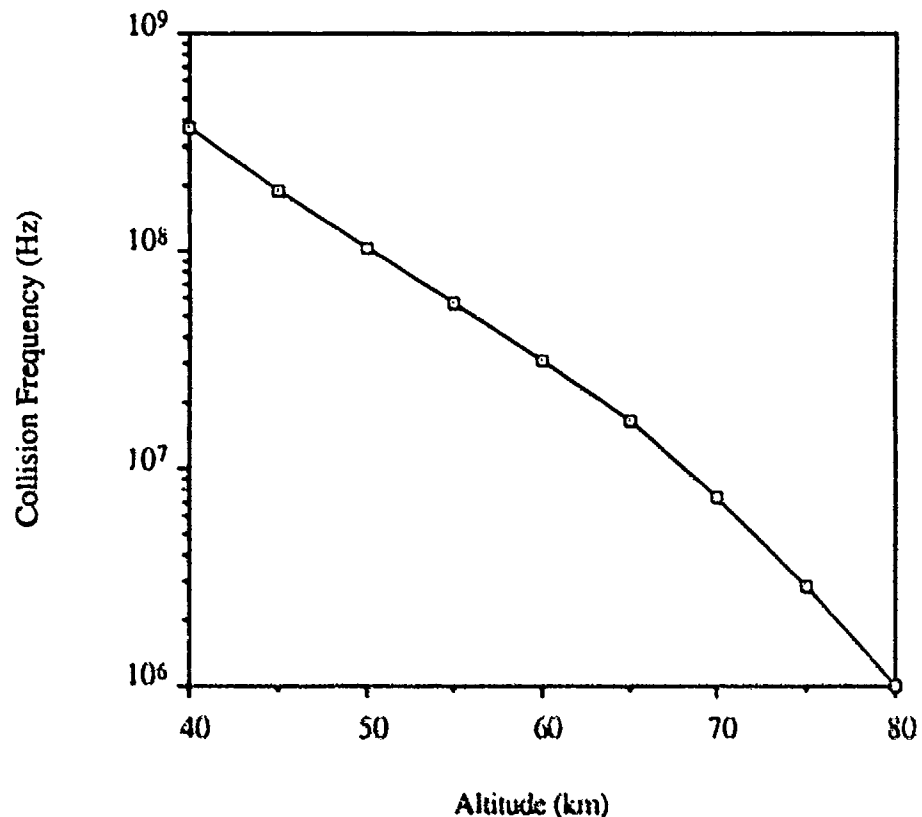


Figure 17. Ambient Electron-Neutral Collision Frequencies

The ambient collision frequencies shown in Figure 17 represent an important restriction on the altitude of the patch for practical AIM systems. For example, if we require that ν_m/ω be less than .1, we can see that a 50 MHz radar system is restricted to patch altitudes above 60 kilometers.

The time required for the patch to cool after formation also varies with altitude. Figure 18 below shows, as a function of altitude, the time required for the electrons to cool (ν_m is within a factor of 2 of its ambient value). Because the fractional ionization is very low, the cooling does not result in

any significant change in the neutral temperature. Note that in terms of the usable lifetime of a patch, which is expected to be of the order of .1 - 1 s, the cooling times are quite short.

In addition to the heating effects during ionization, the cooled plasma may be reheated by the radar wave if its power density is high enough. Since, the time required for reheating is of the order of 1 μ s and decreases at higher powers, the use of short radar pulses to avoid this effect is limited. Figure 19 shows the ratio of v_m after heating to the ambient value for a 50 MHz radar and a patch altitude of 70 kilometers.

Radar patch heating establishes an upper limit on the power density which the radar system places on the patch. As the radar power density exceeds the threshold level for heating (about 0.1 W/m² in the example above), the relationship between incident and reflected power becomes nonlinear. At some point, a maximum reflection is reached, where additional power input causes additional absorption sufficient to cancel the power increase. Above this, additional incident power actually causes the reflected power to decrease. This limiting effect is shown in Figure 20.

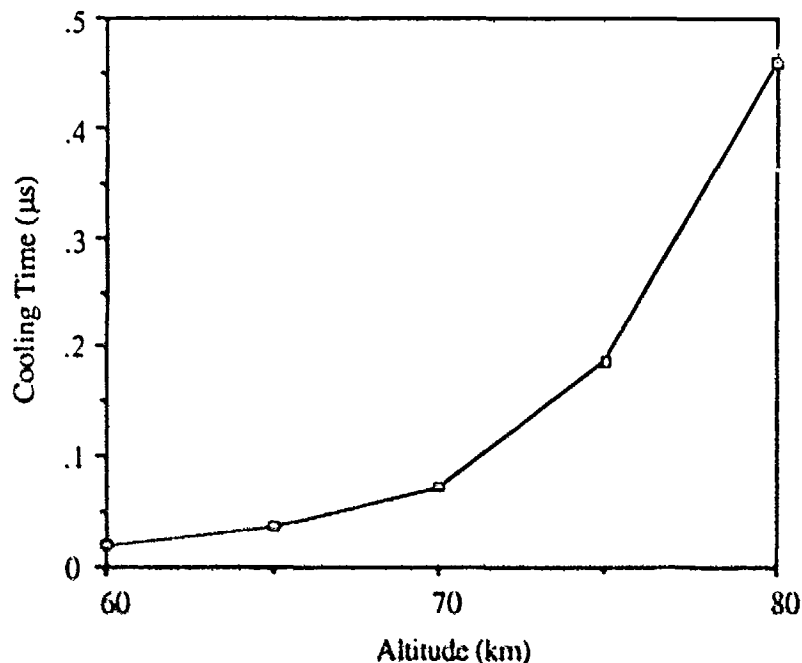


Figure 18. Cooling Time Variations with Altitude

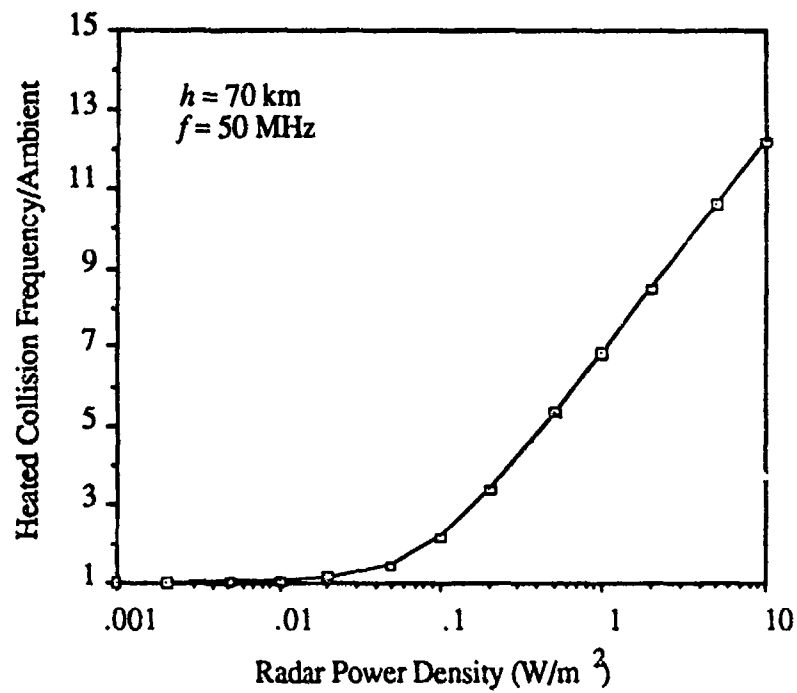


Figure 19. Ratio of Heated ν_m to Ambient

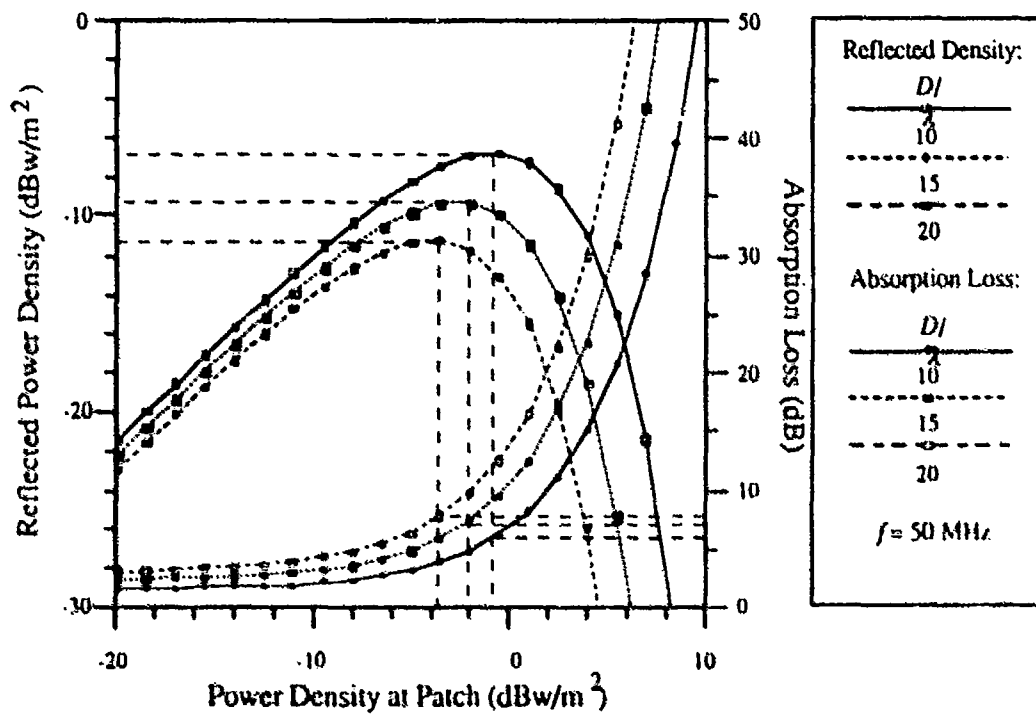


Figure 20. Self-Limiting of Reflected Radar Power by Patch Heating

3.2.2 Dispersion Loss

Random errors during the patch formation process may result in patches which have small-scale departures from the desired shape. The causes of these errors and their expected magnitude have been discussed in Section 2. In this section, we examine the impact of heater beam random positional errors on the radar system.

In order to assess the impact of errors on the ultimate performance of the AIM radar system, we first derive the relationship between rms patch irregularity and the resulting reduction in effective patch gain. Figure 20 illustrates the relevant two dimensional geometry and associated parameters for the AIM cloud.

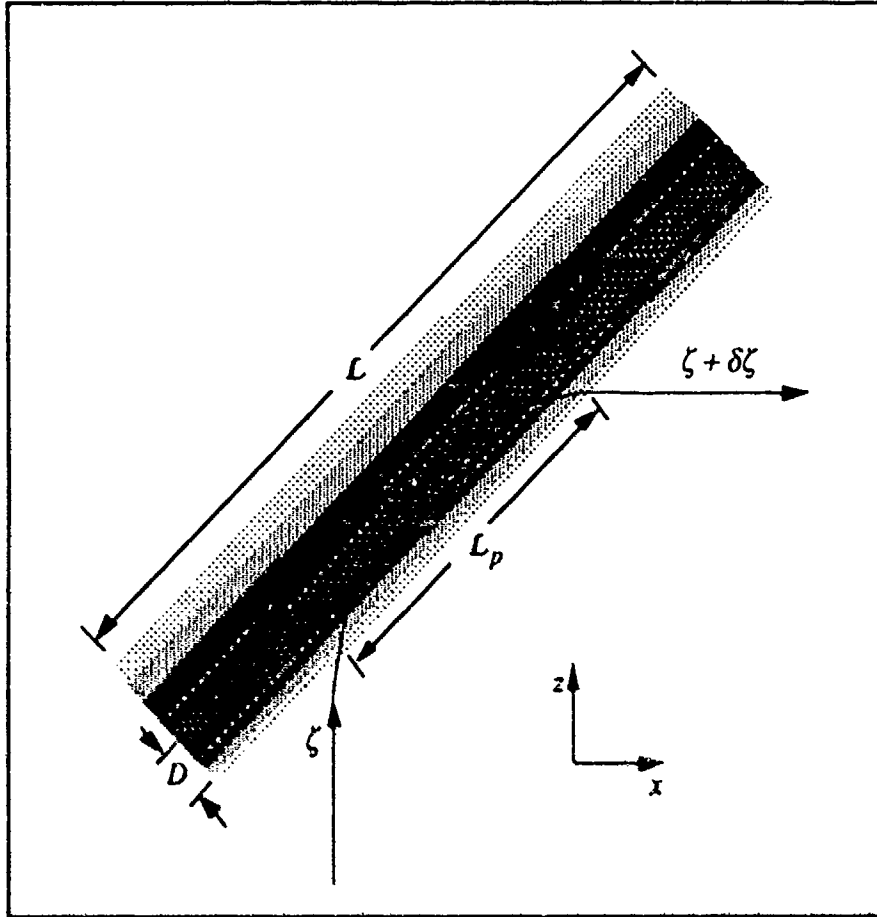


Figure 21. AIM Cloud Geometry

Using the ray path model indicated in Figure 21, the direction of the exiting ray, $\hat{n}(x, z)$ is related to the spatial phase gradient, $\nabla\phi(x, z)$, of the propagating wave by

$$\hat{n}(x, z) = \frac{-\nabla\phi(x, z)}{k}, \quad (50)$$

where $k = 2\pi/\lambda$, is the wave number and $\phi(x, z)$ is the relative phase of the wavefront at location (x, z) . The unit vector in (50), which is locally orthogonal to the surface of constant phase, is given by the direction of the ray leaving the plasma,

$$\eta(x, z) = \begin{bmatrix} \sin(2\zeta + \delta\zeta(x, z)) \\ \cos(2\zeta + \delta\zeta(x, z)) \end{bmatrix}. \quad (51)$$

At any given point in time, the relative phase of the exiting wave at the plasma surface can be found by integrating the phase gradient projected along the direction parallel to the plasma surface. In terms of the parameters indicated in Figure 21, the relative phase along the AIM surface is

$$\begin{aligned} \phi(L) &= \phi(L \sin(\zeta), L \cos(\zeta)) \\ &= \phi_0 - k \int_{L_p}^L \cos(\zeta + \delta\zeta(u \sin(\zeta), u \cos(\zeta))) du \\ &\approx \phi_0 - k(L - L_p) \cos(\zeta) + k \sin(\zeta) \int_{L_p}^L \delta\theta(u \sin(\zeta), u \cos(\zeta)) du. \end{aligned} \quad (52)$$

where

L = the distance along the AIM surface (in the plane of inclination),
 L_p = the distance from the point of entry to the point of exit, for the unperturbed plasma,
and
 $\delta\zeta(x, z)$ = the direction error of the exiting wavefront at (x, z) .

For a linear plasma profile, D. Mosher [13] has shown that

$$L_p = 4D \cot(\zeta) \quad (53)$$

where D is the patch depth (distance from the ambient electron density to a plasma frequency equal to the radar frequency). In the case of the linear electron density profile, Mosher also shows that the direction of the exiting wave front is related to the positional perturbations of the AIM profile by

$$\delta\zeta(L \sin(\zeta), (L \cos(\zeta))) = \frac{1}{2D \cot(\theta)} [\epsilon(L) - \epsilon(L - L_p)]. \quad (54)$$

where $\epsilon(L)$ is the position perturbation relative to the ideal AIM profile, orthogonal to the AIM surface. For the purposes of our analysis, we assume that position errors are on the same order as Δz , thus the approximation $\epsilon(L) = \Delta z(L)$.

The reduction in effective gain from the AIM surface due to the wave front perturbations is given by the integration of the electric field at the plasma surface, which can be reduced to

$$L_d(\zeta) = \frac{1}{(L - L_p)^2} \left| \int_{L_p}^L \exp(j\phi(l) - jk(L - l)\cos(\zeta)) dl \right|^2. \quad (55)$$

where L is the length of the AIM surface, the phase term is compensated relative to the far-field path length in the direction of the maximum gain, and integration is performed over the extent of the AIM surface associated with an exiting wave front. Substituting equation (52) into (55) and simplifying gives

$$L_d(\zeta) = \frac{1}{(L - L_p)^2} \left| \int_{L_p}^L \exp(j\delta\phi(l)) dl \right|^2, \quad (56)$$

where

$$\delta\phi(l) = k \sin(\zeta) \int_{L_p}^l \delta\zeta(u \sin(\zeta), u \cos(\zeta)) du. \quad (57)$$

Since $L_d(\zeta)$ is a function of $\Delta z(l)$ and Δz has been modelled as a random perturbation, $L_d(\zeta)$ is best characterized through its statistical moments. The first order moment is found by taking the expected value as follows:

$$\begin{aligned} E\{L_d(\zeta)\} &= \frac{1}{(L - L_p)^2} \int_{L_p}^L \int_{L_p}^L E\{\exp(j\delta\phi(u) - j\delta\phi(v))\} du dv \\ &= \frac{1}{(L - L_p)^2} \int_{L_p}^L \int_{L_p}^L \exp\left(-\frac{1}{2} R_\phi(u, v)\right) du dv. \end{aligned} \quad (58)$$

where

$$\begin{aligned} \frac{1}{2} R_\phi(u, v) &= E\{|\delta\phi(u) - \delta\phi(v)|^2\} \\ &= \frac{k^2 \sin^2(\zeta) L_p}{2D^2 \cos^2(\zeta)} \int_{L_p}^u \left(1 - \frac{\tau}{L_p}\right) \{R_d(\tau) - R_d((u - v) + \tau)\} d\tau. \end{aligned} \quad (59)$$

In (59), $R_d(\tau)$ is the autocorrelation function of $\varepsilon(l)$, or in our case of $\Delta z(l)$.

Therefore, given a statistical model for the AIM positional errors, the impact of these errors can be related to a corresponding reduction in the unperturbed patch gain. This loss in gain can subsequently be expressed in terms of its impact on the overall radar detection performance. In order to quantify the loss, we assume an exponential autocorrelation for $\epsilon(\mathbf{l})$,

$$\begin{aligned} R_{\epsilon}(\tau) &= E\{\epsilon(\mathbf{l} + \tau)\epsilon(\mathbf{l})\} \\ &= \sigma_{\epsilon}^2 \exp(-.69(\tau/L_c)^2), \end{aligned} \quad (60)$$

where σ_{ϵ}^2 is the rms location error and L_c is the 50% correlation distance. Equations (60) and (59) can be substituted into (58) and integrated numerically to determine the loss in patch gain as a function of the magnitude and correlation length of patch roughness.

In order to assess the overall impact of AIM related losses on the radar performance, the dispersion factor, (58), and absorption factor, (49), are multiplied to obtain a combined one-way AIM loss factor. In considering the two components of this combined loss, we see that as the patch depth, D , is increased the dispersion loss decreases (due to increased averaging), while the absorption loss increases. This phenomenon introduces a trade-off between the two competing loss mechanisms, resulting in an optimal AIM density gradient for a given set of heater/radar design parameters. In comparing Figure 9 with Figure 15 it is apparent that a heater step size of 1/4 beamwidth will provide sufficient AIM smoothness, so that the limiting factor determining beam dispersion will be the heater control errors shown in Figure 15. Figure 22 illustrates the loss trade-off between absorption and beam dispersion as a function of patch depth. In this figure the electron density profile is assumed to be linear with altitude and the patch depth is measured as the distance from the ambient density to the plasma density corresponding to the critical density (i.e. $\omega_p = \omega$).

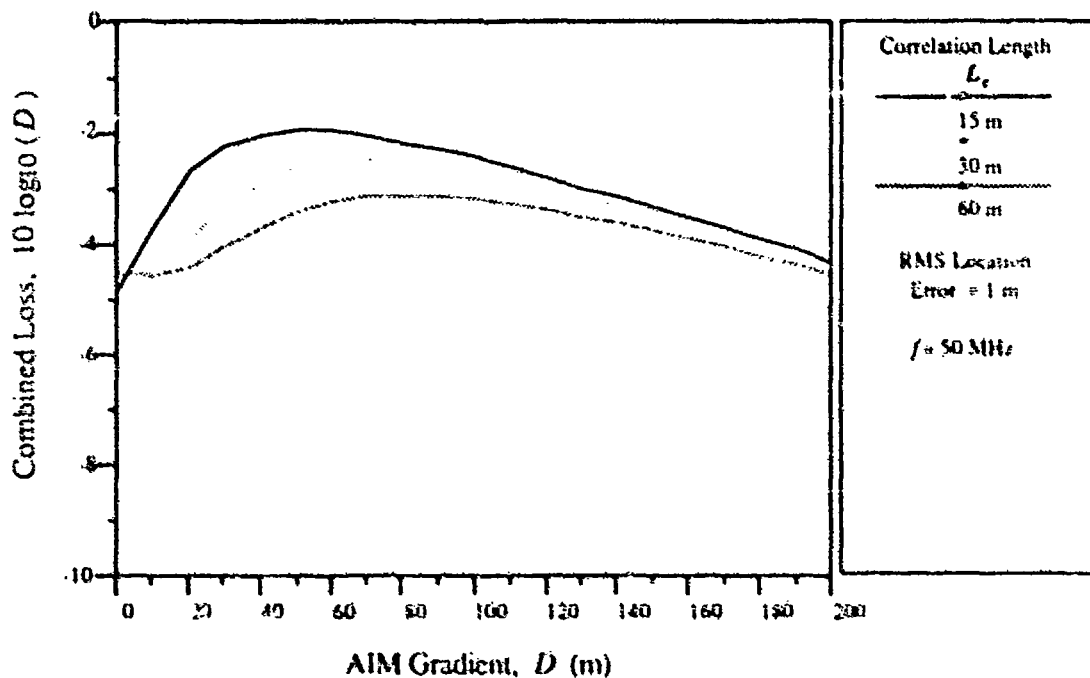


Figure 22. Typical Trade-off For AIM Losses vs Depth of AIM Cloud

3.3 AIM Lifetime and Wind Effects

3.3.1 AIM Lifetime

The time of utility of the AIM cloud is controlled by two physics considerations. The first of these is the cooling rate of the electrons following formation of the cloud. The reason for this is that the fractional absorption of the radar signal is high for energetic electron distributions such as required for the formation of AIM clouds. Following the ionizing heater pulse the electron distribution relaxes in energy by first exciting optical lines and subsequently vibrational and rotational levels of N_2 . Cooling rate estimates are of the order of 10^{-5} sec and are consistent with laboratory experiments [14]. Further analysis of the cooling processes is planned using the Fokker-Planck code. The useful life of the AIM cloud starts following the electron relaxation, since at this point the fractional absorption of the radar signal is minimized.

The end of the AIM cloud useful lifetime (the second physics consideration) is controlled by either local density decay processes or by non-local transport process. For the range of altitudes under consideration (60-80 km) the dominant transport process is related to neutral winds. Electron diffusion is extremely weak since it is ambipolar. Therefore, lifetime estimation has concentrated on the local decay processes due to their shorter time scale. Previous work on the subject (Lombardini, [17] and Gurevich, [16]) identified the three-body attachment process as the cause of the electron density decay of the electron distribution after it has relaxed in energy, which involves two O_2 molecules and one electron. The time scale for this process is

$$t_a = .5 \left(\frac{10^{15}}{N_{O_2}} \right)^2 \text{ s.} \quad (61)$$

where N_{O_2} is the neutral density of O_2 molecules ($\#/cm^2$). Therefore, depending on altitude, it is of the order of .01-1 sec. During a review of the literature, it was noted that in several laboratory experiments, both in the US and USSR, in which the decay of plasma due to local processes was observed [17 - 21] the plasma lifetime was much longer than expected by the value of t_a given above. Furthermore the lifetime scaled with the square of the plasma density square, indicating recombination as a dominant effect. Finally the lifetime had a dependence on the energy expended in producing the discharge. All of the above indicate that detachment due to the interaction of excited N_2 and O_2 molecules with O^+ was balancing three body attachment. This resulted in recombination becoming the dominant plasma loss process. For this to occur sufficient energy should be pumped and stored in vibrational N_2 , thereby accounting for the dependence of the plasma lifetime on the energy expended. In this case the decay time will be given by either recombination or decay of the vibrational states of O_2 which are substantially longer (tens of seconds).

3.3.2 Wind Effects

Because the AIM radar system relies on Doppler processing for clutter rejection, the frequency-domain effects of the reflection process are important. Three major causes of frequency-domain modifications have been identified: patch motion, wind shear, and turbulence. It is important to note that all three of these effects are driven by motions of the neutral atmosphere; because of the very low fractional ionization, 10^{-7} or less, and the relatively high neutral density, plasma oscillations are expected to be very heavily damped and have negligible effect on the reflected signal.

As soon as it is created, the ionized region will move with the neutral atmosphere in which it is embedded. This motion will cause a doppler shift in the signal reflected from the patch, which must be compensated by the radar signal processor. The situation is similar to that encountered in an airborne MTI radar, and signal processing techniques for these situations are well developed. It is not anticipated that motion of the patch as a whole, regardless of the wind speed, will degrade the performance of the system.

If a wind shear exists at the point where the patch is created, the patch will not only move, but be altered in orientation and shape. Because vertical shear is generally much more severe than horizontal shear, it is expected to be the dominant source of shear-induced doppler effects. The vertical extent of the patch is typically 300-600 meters; at altitudes of 70 kilometers, vertical shears of as much as $0.05\text{-}0.07 \text{ sec}^{-1}$ are known to exist. (This figure represents the 1% probability maximum shear at Cape Canaveral, from [22].)

This worst-case situation represents a wind velocity change of 15-40 m/s over the vertical extent of the patch, which corresponds to a rotation of 0.7-3.6 degrees per second. This will cause a change in the direction of the reflected beam of 1.4-7.2 degrees per second. Although this has minor effect on the pointing of the beam, it does impose a scanning modulation on the target signal given by

$$\sigma_f = 0.265 \frac{\varphi_{\text{scan}}}{\phi} \quad (62)$$

where σ_f is the frequency deviation of the power spectrum in Hz, φ_{scan} is the scanning rate in degrees per second, and ϕ is the beamwidth in degrees. The maximum frequency spread for the example system discussed above, for which $\varphi_{\text{scan}} = 12^\circ$, is 0.16 Hz. If the coherent integration time for the radar system is less than 6 seconds, the frequency resolution of the system will be too coarse to detect this modulation. For a radar frequency, f , this frequency deviation corresponds to a velocity deviation of

$$\sigma_v = \frac{c \sigma_f}{2 f} \quad (63)$$

which for our example equals 0.48 meters per second. This is the worst-case frequency spread due to shear for the example system; because it is equal to the velocity spread of a calm sea, it would have a slight effect on clutter rejection for targets over sea. In general, the impact of shear induced scanning modulation is expected to be slight.

3.4 Faraday Rotation

Depending on the geographical location and orientation of the patch, the geomagnetic field will cause some amount of Faraday rotation of the polarization of the reflected radar signal. In some cases, such as a system viewing targets over land, this may be of little importance. As discussed in Section 3.1 scattering characteristics of sea clutter are strongly polarization dependent. Figure 23 shows the HF vertical and horizontal co-polarization cross sections (σ_{vv} and σ_{hh} respectively) for a moderate level sea state, based upon a widely accepted model for backscatter from the sea [23]. These curves show σ_{hh} to be on the order of 20 dB down from σ_{vv} . Therefore, the preferred polarization for reducing sea clutter returns is a linear horizontal electric field. From

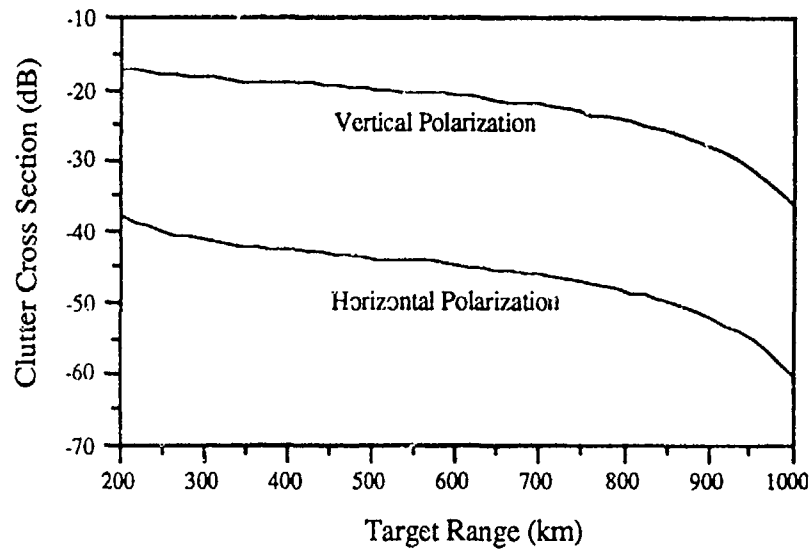


Figure 23. Sea Clutter Cross Sections for a Moderate Sea State¹

Equation (48) we see that as long as the Faraday rotation can be kept to less than 10% (ie. $\gamma_p < .1$) the horizontal backscatter will be the dominant clutter return. This assessment assumes that the polarization separation is limited by the rotation in the AIM, rather than at the transmit and receive channels.

In modeling Faraday rotation, it is necessary to employ a vector wave equation to determine the change in the polarization of the incident wave. The approach selected follows that of Budden, [24], i.e. the calculation of the reflection coefficient rather than the electric field vector to avoid singularities at the reflection point.

In this approach, a vacuum reflection coefficient matrix \mathbf{R} is defined to be

$$\begin{bmatrix} E_{hi} \\ E_{vi} \end{bmatrix} = \mathbf{R} \begin{bmatrix} E_{hr} \\ E_{vr} \end{bmatrix}. \quad (64)$$

Where E_h and E_v are the equivalent vacuum fields at the point where \mathbf{R} is evaluated, and the i and r subscripts indicate incident and reflected waves. The \mathbf{R} matrix indicates the degree to which horizontally polarized incident waves are transformed into vertically polarized reflected waves, and vertically polarized incident are transformed into horizontally polarized reflected, by Faraday

rotation. A complex matrix differential equation for \mathbf{R} in terms of altitude may be derived [22].

$$2j \frac{\partial \mathbf{R}}{\partial z} = \mathbf{w}_{21} + \mathbf{w}_{22} \mathbf{R} - \mathbf{R} \mathbf{w}_{11} - \mathbf{R} \mathbf{w}_{12} \mathbf{R}, \quad (61)$$

where the \mathbf{w} 's are matrix functions of the plasma properties at that altitude and the intensity and orientation of the magnetic field. This set of equations may be solved using any of the various

¹ Cross section models taken from [23].

approaches for ordinary differential equations; in this case, an adaptive altitude step Runge-Kutta method was used.

Computations using typical profiles produced by simulations of the plasma formation process show rotations of as much as 2-3 radians for the worst-case location and patch orientation. In these cases, it may be necessary to precompensate for Faraday rotation by adjusting the polarization of the transmitted signal. Because the amount of rotation depends only on the depth, location, and orientation of the patch, the amount of compensation required can be computed or determined by experiment and applied each time a patch is created. It is important to note that any AIM radar system which scans in azimuth, and which uses polarization control to take advantage of the difference in sea reflectivity, must already have the ability to transmit varying polarizations; so using this capability to compensate for Faraday rotation does not add additional complexity to the system.

4.0 Projected Threat and AIM System Performance

4.1 The Cruise Missile Threat

In order to quantify the potential performance of an AIM based system, a specific surveillance mission and associated threat was selected. Because of the potential use of this type of system as an adjunct to a traditional skywave OTH radar and the importance of the mission, we have selected the continental United States strategic defense as the candidate mission, and the corresponding threat is a low-flying air or sub launched cruise missile. Selection of this mission and threat presents a number of challenging problems.

First, the surveillance environment consists primarily of long-range (beyond-the-horizon) air space over the sea. In order to provide OTH coverage, the AIM will be created at approximately 70 km altitude, giving a down looking beam. The corresponding grazing angle will vary from 0° at the AIM horizon (~ 1100 km) to 15° at 200 km. Therefore, as Figure 23 illustrates sea clutter backscatter will become a limiting factor as the target closes in range. In order to help reduce the sea clutter, a horizontal polarization is preferred (see discussion in Section 3.4).

The second issue to be considered is the relative geometry of a low-flying target over a conducting surface, such as the sea. As is well known, this geometry can give rise to severe multipath nulls. An effective approach to dealing with multipath is the use of frequency diversity. As the transmit frequency is changed, the multipath nulls move in range (with the exception of the first null at the AIM horizon). This effect is illustrated in Figure 24, where a single frequency multipath response is compared to the average response due to a transmit frequency that is hopped between three frequencies: 43 MHz, 49 MHz, and 54 MHz. As these curves illustrate, the use of frequency diversity all but eliminates the multipath nulls.

Finally, the radar cross section characteristics of a cruise missile play an important role in how well the radar will be able to detect and maintain a track on the target. Figure 25 shows a numerically calculated radar cross section of a cruise missile like target. The target consists of a metallic cigar-

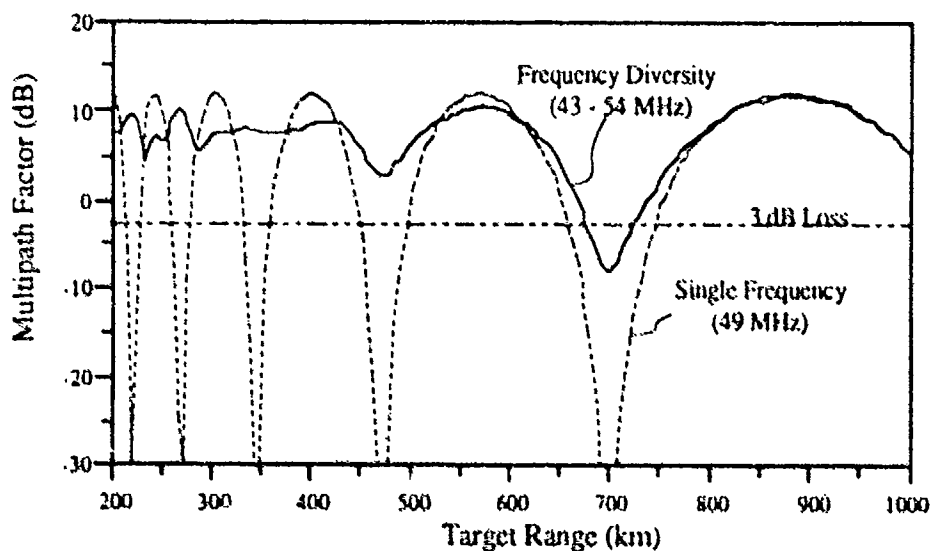


Figure 24. Impact of Multipath Can be Limited by Using Frequency Diversity (50 m Target)

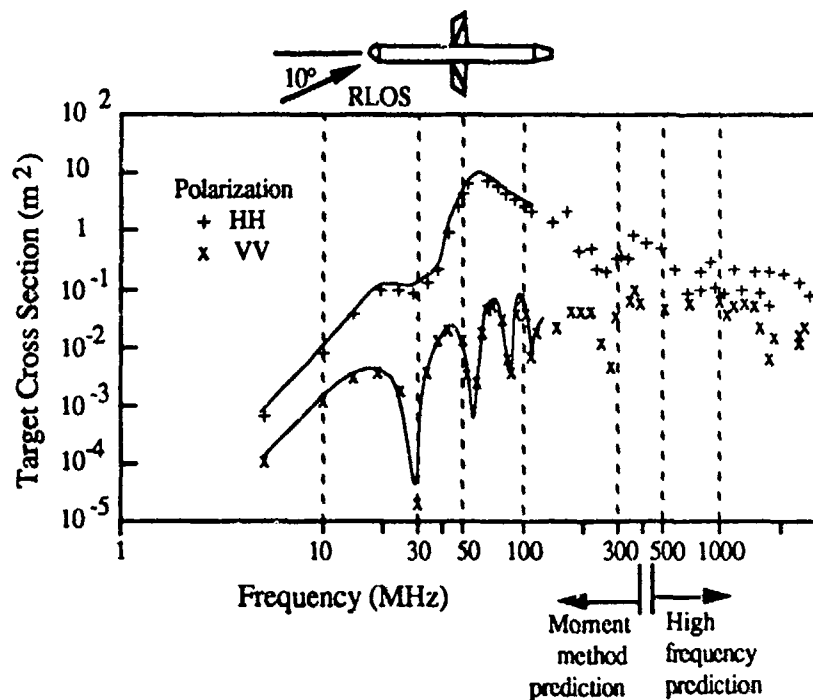


Figure 25. Numerical Model for a Cruise Missile Like Target Illustrates the Advantages of Having Positive Frequency and Polarization Control¹

shaped cylinder with metal fins. The dimensions of the target approximate those of a typical cruise missile. While the resulting cross section calculations do not exactly match those of a real cruise missile, they do give a good indication of the relative dependence upon frequency and polarization. As these curves indicate, resonance occurs in the 50 - 100 MHz range, with a consequent fall off as f^4 below this region (corresponding to Rayleigh scattering). Additionally, for low grazing angle, closing geometries there is a strong dependence on polarization, with horizontal polarization providing from 10 to 20 dB advantage. Therefore, the positive frequency and polarization control offered by AIM can be used to simultaneously exploit the cross section characteristics of both the target and the sea clutter.

4.2 A Baseline System and its Predicted Performance

Baseline Heater:

This section describes the current baseline heater system and describes trade studies that have been performed to arrive at this baseline. There are two rather distinctive approaches for simultaneously obtaining the high ERP, achieving the positive field gradient needed for controlled breakdown, and controlling the plasma cloud with sufficient precision that it may be used for the radar application:

- 1) a large, solid-state phased array, or
- 2) high-power tubes (klystrons, likely) feeding several dishes.

¹ Taken from C. C. Cha, Syracuse Research Corporation [25].

Our current understanding of the phenomenology and the available technology leads us to favor the solid-state approach for the Full Scale Engineering Development system because of its greater controllability, likely lower life cycle costs, and greater reliability. The tube approach is currently favored for an atmospheric proof of principle demonstration because of its lower development cost.

Based on our study of the plasma creation process and associated control requirements, formation of an AIM that will efficiently reflect HF/VHF radar waves requires a heater with baseline design characteristics as follows:

- Heater frequency in the UHF band,
- Moderate (about 10%) frequency agility,
- Effective radiated power of 156 dBW,
- Average radiated power of 2-5 MW,
- Duty cycle of 0.1-5 %, and
- Flexible and accurate control of the E field focus.

The current baseline concept for the heater antenna consists of a large, phased array (about 4 km²) with solid state transmit elements, each radiating at a nominal frequency of 425 MHz (Figure 26). While the number and placement of the antenna elements is still subject to a detailed design, the general trade-off is one of increasing the number of elements (ie. radiating aperture) in order to reduce the required heater energy per AIM cloud. As the array area is filled, it becomes more efficient in terms of placing radiated power at the heater focus, consequently requiring less total radiated power.

To support the requirement for near-field focussing of the heater, each sub-panel will be digitally calibrated and synchronized. Reference signals will be measured by receivers used to provide

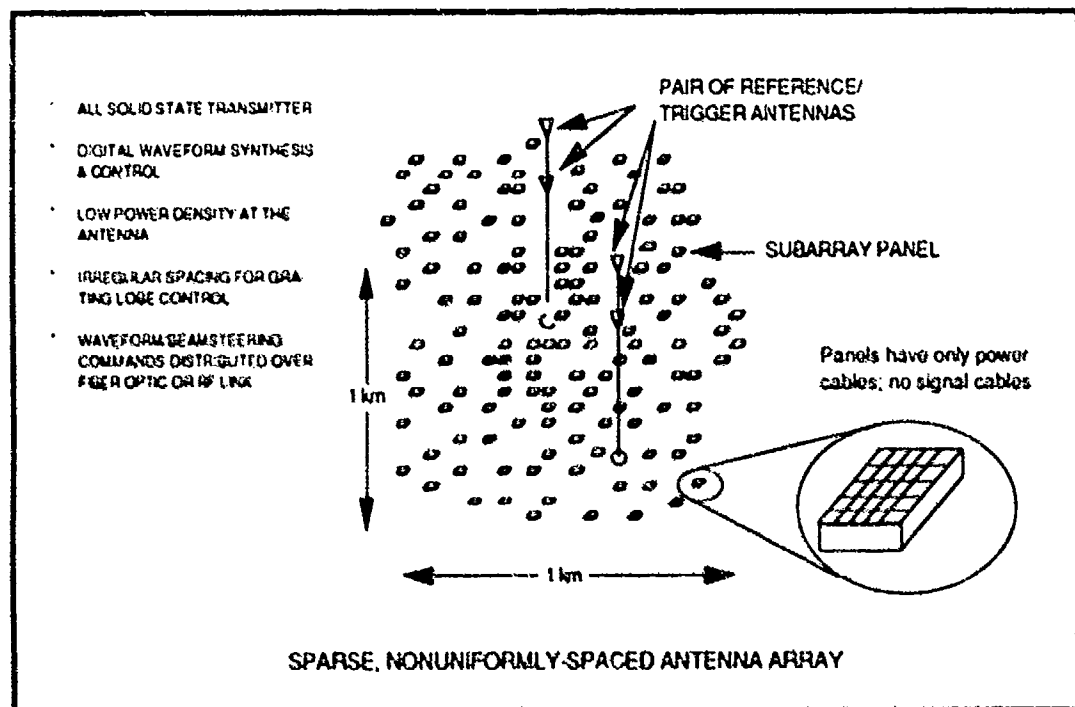


Figure 26. The FSED AIM Heater Phased Array Antenna

calibration for each sub-panel. Digital control and waveform synthesis will provide very accurate synchronization of the transmit waveforms, allowing complete flexibility in synthesizing the field distribution at the breakdown region by specifying the phase and amplitude weights for each sub-panel.

An alternate approach would consist of an array of reflectors up to 25 meters in diameter driven by high powered L or S band klystrons. The number of reflectors may vary from 25 to several thousand depending on the size of the reflector, AIM requirements and output characteristics of the klystron. The number of klystrons may vary from 10 to several hundred depending on their output. A design for a L band klystron with 1 GW output power for a 1 μ s pulse has been proposed. There exists a commercially available L band klystron at 250 MW with a 1 μ s pulse. This array of reflectors would be focused as the baseline concept with digital waveform synthesis and control. The ultimate choice will be determined based on system trade-offs of AIM creation phenomenology, performance requirements, and cost.

Baseline Radar:

The baseline AIM radar consists of a phased array aperture operating in the 30 - 60 MHz range, with an ERP of 98 to 104 dBW. The radar will operate with a frequency-swept FM pulsed waveform, where the pulse width is chosen to match the 540 km two-way propagation time, from the radar to the initial range of surveillance. This will provide maximum average power, compressed range resolution, and co-location of the transmit and receive aperture. Table 5 summarizes the pertinent radar/patch parameters for 25 MHz and 50 MHz baseline designs. These designs will provide a 360° azimuth scan, with a 1.5° to 3° azimuth beamwidth and range coverage of 200 to 1000 km for a low flying target (50 m altitude). Scan update times for 360° coverage will be on the order of 1 to 4 minutes, depending upon AIM lifetimes and azimuth beam width.

Table 5. Two Baseline Radar Configurations

System Parameters	HF AIM	VHF AIM
Average Power	1.2 MW	1.2 MW
Antenna Aperture (Gain)	250 x 250 m (37 dB)	250 x 250 m (43 dB)
Frequency	25 MHz	50 MHz
Bandwidth	10 kHz	100 kHz
Effective Noise Temperature	13,000° K	7,000° K
System Losses	10 dB	10 dB
Patch Parameters		
Size	1.5 x 3.0 km	1.4 x 2.0 km
Altitude	70 km	70 km
Inclination	40° to 45°	40° to 45°
Propagation Loss	4 dB (one-way)	5.5 dB (one-way)
Relative Polarization (VV/HH)	-24 dB	-28 dB
Beam Dispersion	1.5° az, 15° el	1.5° az, 15° el

Baseline Performance:

Figure 27 indicates the expected performance of the two baseline radars shown in Table 5, using AIM against targets at 200 - 1,000 km ranges. These curves illustrate the sensitivity of the radar detection performance in a moderate level sea clutter and in noise. All AIM and system related losses have been included in the analysis. The minimum detectable target is defined as the

minimum radar cross section required for a probability of detection exceeding 90% with a false alarm rate of 10^{-3} (~ 100 pre-tracking false alarms per scan). As can be seen, the VHF radar has over 30 dB margin against the target illustrated in Figure 25.

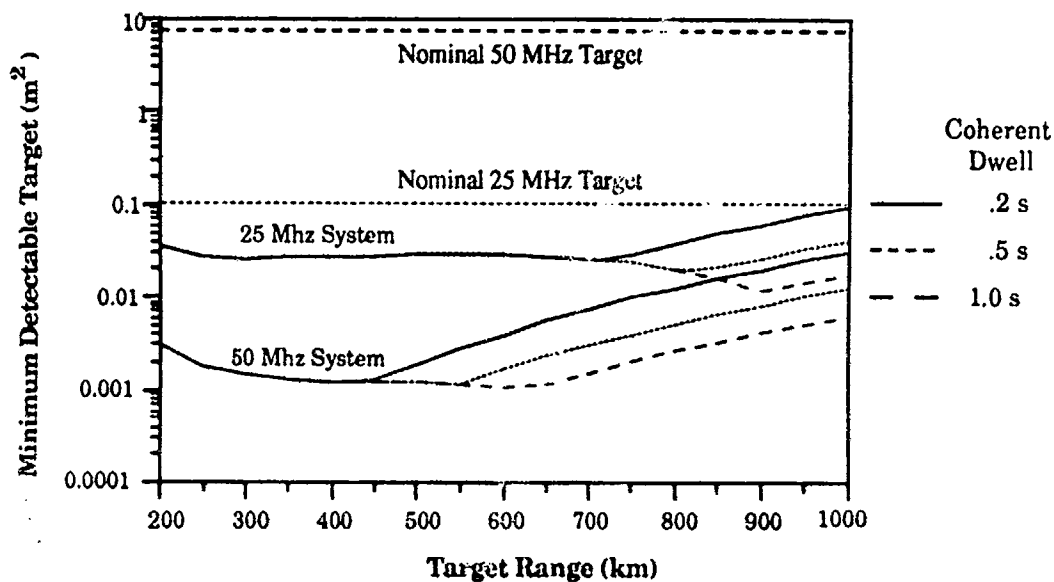


Figure 27. AIM Detection Performance Provides 30 dB Margin at VHF

5.0 Summary

As the results in this paper have indicated, the operational geometry and radar characteristics of an AIM based surveillance radar can provide system performance that is well suited to the long-range detection and tracking of small, low-flying targets, as exemplified by the ALCM and SLCM threats. The performance characteristics of a stand-alone AIM system are highlighted by

- 200-1200 km detection/tracking ranges (depending on target altitude),
- azimuth coverage over 360° , or any fractional sector,
- beam grazing angles of less than 10 degrees (for 65-80 km high AIM),
- good horizontal polarization control,
- operation at RFs in the HF to low VHF (to about 90 MHz), and
- 90% detection probability of a -25 dBsm target at 1,000 km range, providing 30 dB of margin for typical low observable threat projections at VHF.

In the case of strategic defense of the continental United States, an AIM system can provide an important augmentation to current and planned deployment of more traditional skywave over-the-horizon radars. AIM enhances the overall performance of these OTH radars by

- filling in the range hole that exists out to about 1000 km due to the minimum HF hop distance,
- mitigation of auroral effects in polar directed surveillance sectors,
- sustained operation through periods of increased sunspot activity and other ionospheric degradations,
- availability of the upper end of the HF spectrum during the diurnal ionospheric cycle, and
- improved detection of LO targets through frequency selection and positive polarization control.

The basic questions concerning the feasibility of the AIM concept all relate to how reliably one can create the AIM within tolerances necessary for useful reflection of the radar signal. Issues that directly impact AIM utility (size, shape, orientation, uniformity, smoothness, peak electron density, steepness of the density gradient, and density lifetime) have been addressed above. While some uncertainties still remain, efforts to-date have reduced these uncertainties to the extent that there appears to be no phenomenological issue preventing realization of the AIM concept. This is based upon extensive physics studies and system trade-off considerations. Results of these investigations indicate that the AIM can be created using current technology, with the necessary radar reflective characteristics to provide wide area surveillance and early detection and tracking of the ALCM/SLCM threat of the future. Based on these results, the next phase of effort should include the careful design and planning of an atmospheric demonstration of the AIM concept.

6.0 Acknowledgements

The authors would like to express their gratitude to the following people, who have contributed to conceptualization and assessment of AIM. Adam Drobot, Dennis Papadopoulos, Ramy Shanny, Sherman Karp, and John Allen have played a direct technical role, ranging from the initial formulation of the AIM concept to the feasibility assessment of AIM as a viable OTH radar concept. Larry Marple provided the initial concepts for digital heater control. Paul Kossey has provided both programmatic direction, as the GL program manager, as well as valuable technical guidance. Finally, a number of experts have reviewed AIM and made important suggestions, which have served to help identify and resolve the critical issues relative to the viability of the AIM concept. These contributors include: Jon Don Carlos, Hal Guthart, Ed Key, Allan Peterson, Larry Sweeny, and Ike Weissman.

7.0 Bibliography

1. W. Fenster, "The Application, Design, and Performance of Over-the-Horizon Radars," *International Conference RADAR-77*, pp 36-40, Oct. 25-28, 1977, IEEE (London).
2. J.M. Headrick, J.F. Thomason, and S.J. Anderson, "A Critical Appraisal of Alternative Designs for HF Over-the-Horizon Radars," *Record of the Thirty-Third Annual Tri-Service Radar Symposium*, The Naval Postgraduate School, Monterey, Ca., 24 June 1987.
3. J.M. Headrick and M.I. Skolnik, "Over-the-Horizon Radar in the HF Band," *Proceedings of the IEEE*, Vol. 62, No. 6, June 1974.
4. A. Drobot, K. Papadopoulos, and R. Hirsch, "Artificial Ionospheric Ionization for Radar Applications," Presentation to Project Forecast II, U. S. Airforce, February 1987.
5. A.V. Gurevich, *Nonlinear Phenomena in the Ionosphere*. Springer-Verlag, N.Y. 1978.
6. K. Papadopoulos, et al., "Physics of Ionospheric Breakdown for AIM Applications," *Proceedings of the 46th Symposium of AGARD's Electromagnetic Wave Propagation Panel*, Bergen, Norway, May 1990.
7. R. D. Short, et al. "Physics Studies in Artificial Ionospheric Mirror (AIM) Related Phenomena," GL-TR-90-0038, Final Report, Contract F19628-87-C-0127. ADA227112
8. S. P. Blood, et al., "Studies of High Latitude Mesospheric Turbulence by Radar and Rocket 2: Measurements of Small Scale Turbulence," *Journal of Atmospheric and Terrestrial Physics*, Vol. 50, No. 10/11, 1988.
9. C. A. Greene and R. T. Moller, "The Effect of Normally Distributed Random Phase Errors on Synthetic Array Gain Patterns," *IRE Transactions on Military Electronics*, Vol. MIL-6, No. 2, April 1962, pp 130-139.
10. M. I. Skolnik, Editor, *Radar Handbook*, McGraw-Hill, New York 1970
11. S. Karp, R. M. Gagliardi, S. E. Moran, and L. B. Stotts, *Optical Channels*, Plenum Press, New York, 1988.
12. W. Case and P. Sprangle, *Private Communication*, 1988.
13. D. Mosher, *Private Communication*, 1988.
14. L. Christophorou (Editor), *Electron-Molecule Interactions and Their Applications*, vol. 1-2, Academic Press, 1984.
15. P. Lombardini, "Alteration of the Electron Density of the Lower Ionosphere," *Radio Science*, G9D, 1965.
16. A. V. Gurevich, "An Ionized Layer in a Gas (in the Atmosphere)," *Soviet Physics - USP.*, 23, 12 (1980).
17. A. V. Eletski and B. M. Smirnov, "Dissociative Recombination of Electron and Molecular Ions," *Kurchatov Institute of Atomic Energy, Usp. Fiz. Nauk* 136, 25-59 (January 1982).

18. A. N. Vasil'eva, I. A. Grishima, A. S. Kovaler, V. I. Ktitorov, N. A. Loginov, and A. T. Rakhomov, "Plasma Decay in O_2 - N_2 Mixtures," *Soviet Journal Plasma Physics*, 3, 1977.
19. A. L. Vikharev, O. A. Ivanov, and A. N. Stepanov, "Decay of the Plasma of a Pulsed Microwave Discharge in Intersecting Wave Beams," *Soviet Journal Plasma Physics*, 10, 4 (1984c).
20. W. L. Nighan and W. J. Wiegand, "Influence of Negative-Ion Process on Steady State Properties and Striations in Molecular Gas Discharges," *Physics Review A*, 10, 1974.
21. A. P. Napartovich, V. G. Naunov, and V. M. Shoshkov, "Plasma Decay in a Glow Discharge in a Constant Electric Field," *Soviet Journal Plasma Physics*, 1, 1975.
22. A. S. Jursa (Editor), *Handbook of Geophysics and the Space Environment*, Air Force Geophysics Laboratory, Air Force Systems Command, 1985, (Doc. No. ADA 167000).
23. D. Barrick, "First Order Theory and Analysis of MF/HF/VHF Scatter from the Sea," *IEEE Transactions on Antennas and Propagation*, vol. AP-20, no. 1, January 1972.
24. K. G. Budden, *The Propagation of Radio Waves*, Cambridge University Press, 1985.
25. Cha, C. C., "An RCS Analysis of Generic Airborne Vehicles Dependence on Frequency and Bistatic Angle," *Proceedings of IEEE National Radar Conference*, Ann Arbor, Michigan, April 1988.